



THE MAJOR GEOEFFECTIVE SOLAR ERUPTIONS OF 2012 MARCH 7: COMPREHENSIVE SUN-TO-EARTH ANALYSIS

S. PATSOURAKOS¹, M. K. GEORGIOULIS², A. VOURLIDAS³, A. NINDOS¹, T. SARRIS⁴, G. ANAGNOSTOPOULOS⁴, A. ANASTASIADIS⁵,
G. CHINTZOGLOU⁶, I. A. DAGLIS⁷, C. GONTIKAKIS², N. HATZIGEORGIOU⁸, A. C. ILIOPOULOS⁴, C. KATSAVRIAS⁷, A. KOULOUMVAKOS¹,
K. MORAITIS², T. NIEVES-CHINCHILLA⁹, G. PAVLOS⁴, D. SARAFPOULOS⁴, P. SYNTHELIS^{2,7}, C. TSIRONIS^{5,10}, K. TZIOTZIOU²,
I. I. VOGIATZIS⁴, G. BALASIS⁵, M. GEORGIOU⁷, L. P. KARAKATSANIS⁴, O. E. MALANDRAKI^{4,5}, C. PAPADIMITRIOU^{5,7}, D. ODSTRČIL⁶,
E. G. PAVLOS⁴, O. PODLACHIKOVA¹, I. SANDBERG⁷, D. L. TURNER¹¹, M. N. XENAKIS⁴, E. SARRIS⁴, K. TSINGANOS^{12,7},
AND L. VLAHOS¹⁰

¹ University of Ioannina, Department of Physics, Section of Astrophysics, Ioannina, Greece

² Research Center for Astronomy and Applied Mathematics, Academy of Athens, Athens, Greece

³ Space Physics Division, Applied Physics Laboratory, Johns Hopkins University, Laurel, MD, USA

⁴ Democritus University of Thrace, Department of Electrical and Computer Engineering, Xanthi, Greece

⁵ IASARS, National Observatory of Athens, GR-15236 Penteli, Greece

⁶ School of Physics, Astronomy and Computational Sciences, George Mason University, 4400 University Drive, MSN 6A2, Fairfax, VA 22030, USA

⁷ Department of Physics, University of Athens, Greece

⁸ University of California, Berkeley, Space Sciences Laboratory, Berkeley, CA 94720-7450, USA

⁹ IACS/CUA at NASA Goddard Space Flight Center Heliospheric Physics Lab, Greenbelt, MD 20771, USA

¹⁰ University of Thessaloniki, Department of Physics, Thessaloniki, Greece

¹¹ University of California, Los Angeles, CA 90095-1567, USA

¹² National Observatory of Athens, Athens, Greece

Received 2015 June 7; accepted 2015 November 18; published 2016 January 19

ABSTRACT

During the interval 2012 March 7–11 the geospace experienced a barrage of intense space weather phenomena including the second largest geomagnetic storm of solar cycle 24 so far. Significant ultra-low-frequency wave enhancements and relativistic-electron dropouts in the radiation belts, as well as strong energetic-electron injection events in the magnetosphere were observed. These phenomena were ultimately associated with two ultra-fast ($>2000 \text{ km s}^{-1}$) coronal mass ejections (CMEs), linked to two X-class flares launched on early 2012 March 7. Given that both powerful events originated from solar active region NOAA 11429 and their onsets were separated by less than an hour, the analysis of the two events and the determination of solar causes and geospace effects are rather challenging. Using satellite data from a flotilla of solar, heliospheric and magnetospheric missions a synergistic Sun-to-Earth study of diverse observational solar, interplanetary and magnetospheric data sets was performed. It was found that only the second CME was Earth-directed. Using a novel method, we estimated its near-Sun magnetic field at $13 R_{\odot}$ to be in the range $[0.01, 0.16] \text{ G}$. Steep radial fall-offs of the near-Sun CME magnetic field are required to match the magnetic fields of the corresponding interplanetary CME (ICME) at 1 AU. Perturbed upstream solar-wind conditions, as resulting from the shock associated with the Earth-directed CME, offer a decent description of its kinematics. The magnetospheric compression caused by the arrival at 1 AU of the shock associated with the ICME was a key factor for radiation-belt dynamics.

Key words: solar–terrestrial relations – Sun: corona – Sun: coronal mass ejections (CMEs) – Sun: magnetic fields

Supporting material: animations

1. INTRODUCTION

Current solar cycle 24 has been the weakest since 1906 (e.g., see <http://solarscience.msfc.nasa.gov/predict.shtml>). This cycle succeeded a very deep solar minimum, with various solar, interplanetary (IP), and geomagnetic parameters reaching lower values than in previous cycles. The 61 month sunspot number average for cycle 24 is $\sim 56\%$ of that corresponding to cycle 23 (Gopalswamy et al. 2015a). The M- and X-class flare rate of the *Geostationary Operational Environmental Satellites* (GOES) dropped by $\sim 50\%$ between 2002 and 2012 (Hudson et al. 2014). In addition, coronal mass ejections (CMEs) in cycle 24 are less massive (Wang & Colaninno 2014) and broader (for a given speed) than those of cycle 23 (Gopalswamy et al. 2015a). Cycle 24 has so far seen only two solar energetic particle (SEP) events with ground-level enhancement, many fewer than the 13 events encountered during cycle 23 (Gopalswamy et al. 2015b). The IP total pressure (gas and magnetic), as measured at 1 AU during

cycle 24, is $\sim 40\%$ of the total pressure of the previous cycle (Gopalswamy et al. 2015a). The geomagnetic activity is also significantly reduced during cycle 24. For example, the K_p index in the rising phase of the current cycle reached the lowest levels since the beginning of K_p measurements in 1932, in comparable solar-cycle phases (Richardson 2013). The number of major geomagnetic storms (Dst index $\leq -100 \text{ nT}$) during cycle 24 until now amounts to $\sim 25\%$ of those recorded during the previous cycle (e.g., Richardson 2013; Gopalswamy et al. 2015a). Only one severe geomagnetic storm (Dst index $\leq -200 \text{ nT}$) has been recorded so far in cycle 24 during 2015 March 17, compared with 18 such events during cycle 23 (Zhang et al. 2007). In summary, cycle 24 has been a very “quiescent” cycle in terms of solar, IP, and geomagnetic activity.

Nevertheless, cycle 24 has been marked by a few periods of particularly high solar activity. Intense flaring and ultra-fast CMEs gave rise to very adverse space weather conditions in

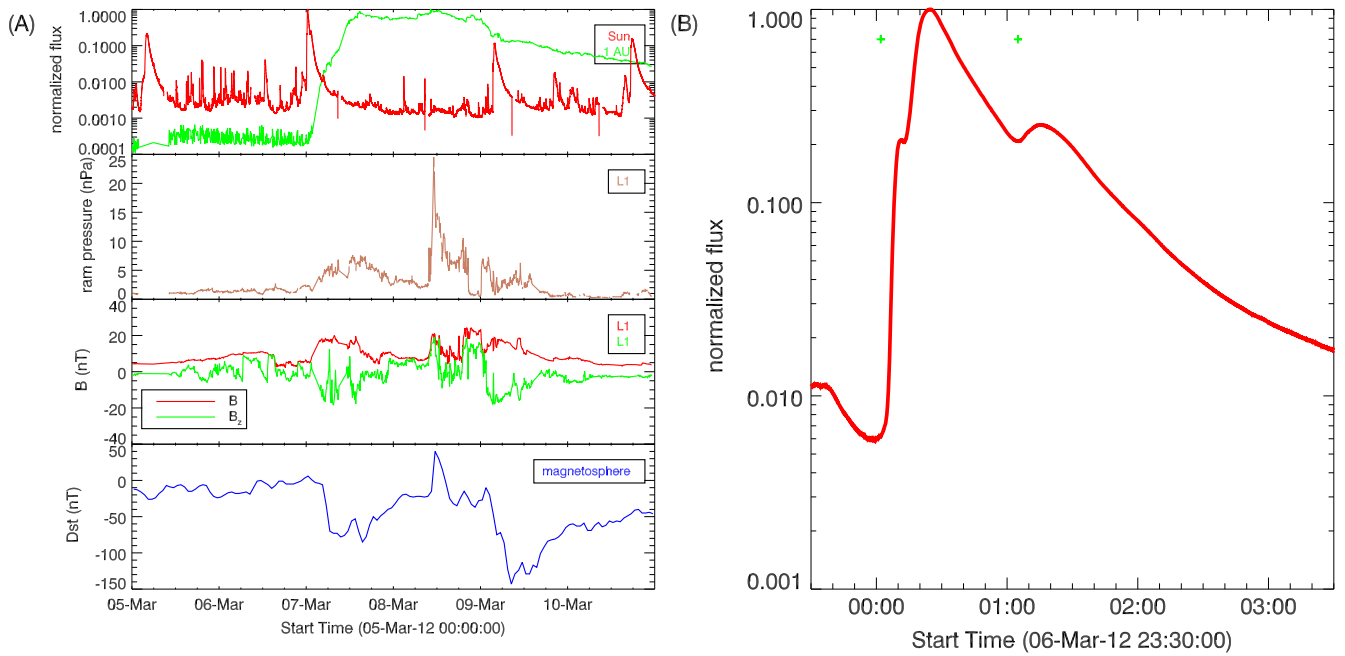


Figure 1. Panel (A): selected observations along the Sun–Earth line during the interval 2012 March 5–11. From top to bottom: *GOES* 1–8 Å SXR (red) and energetic protons with energies >30 MeV (green), solar-wind ram pressure at L1, magnetic field magnitude (red) and B_z (in the geocentric solar ecliptic (GSE) system, green) at L1, Dst index. Panel (B): *GOES* 1–8 Å SXR during the two reported X-class flares. The green crosses correspond to the onsets of the two X-class flares.

geospace and beyond. One such interval of high solar activity, from 2012 March 5 to 11, is linked to the appearance on the solar disk of solar active region (AR) 11429 of the National Oceanic and Atmospheric Administration (NOAA). The most important eruptive activity in this AR took place on March 7, with a barrage of two X-class eruptive flares in rapid succession, associated with two ultra-fast CMEs.

A set of observations from the Sun to the terrestrial magnetosphere in the interval 2012 March 5–11 are shown in panel (A) of Figure 1. They include solar soft X-rays (SXR) and energetic protons (red and green curves in the first plot from the top, respectively), solar wind ram pressure (brown curve in the second plot from the top), magnetic field (magnitude and B_z) at L1 (red and green curves in the third plot from the top, respectively), and Dst index (blue curve in the fourth plot from the top). The impact of the 2012 March 7 solar eruptions in the heliosphere and the geospace was striking. These events generated one of the most intense energetic proton events of 2012 (Kouloumvakos et al. 2015), with near-relativistic electrons seen at Mercury’s orbit by *Messenger* (Lario et al. 2013). They caused the most intense energetic-particle radiation levels during the cruise of the *Mars Science Laboratory* to Mars (Zeitlin et al. 2013). The associated shock(s) drifted across much of the inner solar system and possibly far beyond: more than a year after the 2012 March eruptions, *Voyager 1* detected locally generated electron plasma oscillations during 2013 April at a heliocentric distance of 124 AU. The oscillations were most likely driven by the 2012 March eruptions in NOAA AR 11429 (Gurnett et al. 2013).

Around 35 hr after the onset of the two X-class flares, a strong pressure pulse arrived at 1 AU. A strong southward interplanetary magnetic field (IMF) ensued ~ 9 hr later, indicating the passage of an interplanetary CME (ICME). These two events led to the sudden storm commencement

(SSC) and the onset of the main phase of the second most intense geomagnetic storm of cycle 24 to date, with the Dst index diving to -148 nT (Figure 1, panel (A), bottom plot). For the three-day period in March 8–10, aurorae were observed in northern high-to-middle latitudes. A very strong decrease in cosmic-ray fluxes was observed on the ground, associated with the arrival of the ICME (Mavromichalaki et al. 2013). Overall, the solar eruptive events of 2012 March 7 gave rise to one of the most interesting space weather periods of cycle 24.

The close temporal (onsets within an hour) and spatial (from the same AR) proximity of the two eruptive X-class flares, as well as the eastern location of the source AR, pose a set of challenging questions.

1. Which of the two CMEs, if not both, was Earth-directed?
2. How can an eastern-hemisphere event lead to a geoeffective CME when the sources of most major geomagnetic storms lie close to the central meridian (e.g., Zhang et al. 2007)?
3. What made these events so geoeffective?
4. Can we use solar and coronal observations to obtain estimates of the near-Sun magnetic field of the Earth-directed CME? Note that very few near-Sun observations of CME magnetic fields exist (e.g., Bastian et al. 2001; Jensen & Russell 2008; Tun & Vourlidis 2013).
5. Can we draw causal links and connections between the various observed solar, IP, and magnetospheric phenomena?

We are in a prime position to address these questions because the entire event, from the Sun to Earth’s magnetosphere, was observed by the most comprehensive array of solar, heliospheric, and magnetospheric instrumentation on record. For instance, the *Solar Dynamics Observatory* (SDO; Pesnell et al. 2012) provides multi-wavelength observations

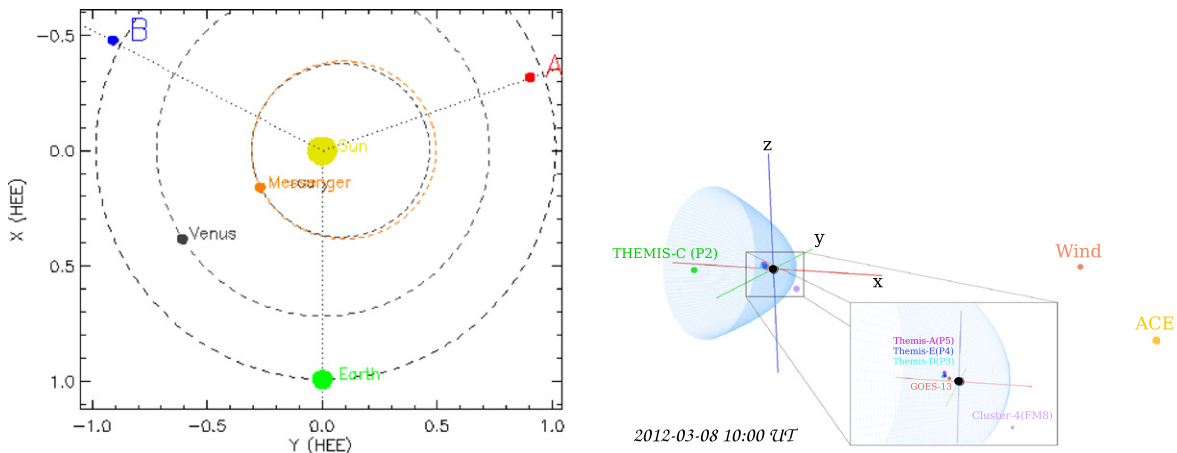


Figure 2. Left panel: observing configuration on 2012 March 7 00:00 UT showing the location of *STEREO B* (blue circle), *STEREO A* (red circle), *Messenger* (orange circle) and Earth (green circle). Right panel: locations of *THEMIS A*, *C*, *D*, and *E*, *GOES-13 ACE*, *Wind* and *Cluster* spacecraft on 2012 March 8 10:00 UT, shortly before the arrival of the pressure pulse associated with the solar eruptions of 2012 March 7. The light-blue bow-shaped structure corresponds to the bow shock with its axes in the GSE system.

with high temporal and spatial resolution of the corona by the Atmospheric Imaging Assembly (AIA; Lemen et al. 2012), complemented by vector magnetograms of the underlying photosphere by the Helioseismic and Magnetic Imager (HMI; Scherrer et al. 2012). The CME propagation from Sun to IP space is monitored by the imagers, coronagraphs, and heliospheric imagers of the Sun–Earth Connection Coronal and Heliospheric Investigation (SECCHI; Howard et al. 2008) aboard the twin *Solar Terrestrial Relationship Observatory* (*STEREO*) spacecraft. Supplementary coronagraphic views are provided by the Large Angle and Spectrometric Coronagraph (LASCO) coronagraphs (Brueckner et al. 1995) aboard the *Solar and Heliospheric Observatory* (*SOHO*) mission. Finally, a fleet of in situ monitors either orbiting around L1 (such as *Wind* measuring plasma (Ogilvie et al. 1995) and magnetic field (Lepping et al. 1995) parameters) or at various places in and around the magnetosphere (such as the five *Time History of Events and Macroscale Interactions* (*THEMIS*) spacecraft (Angelopoulos 2008), *Cluster* (Balogh et al. 1997; Escoubet et al. 1997), and the *Geostationary Operational Environmental Satellites* *GOES-13* and *GOES-15*) supply comprehensive views of the geospace impact of the solar eruptions. Figure 2 provides an overview of the configuration of the various observatories used in this study.

In this article we present an overview of the two eruptive flares (Section 2), use geometrical fittings of coronagraphic observations to determine which of the associated CMEs was Earth-directed and derive its magnetic helicity budget (Section 3), deduce its near-Sun magnetic field, using a novel method, and extrapolate its magnetic field and kinematics to 1 AU (Section 4), and present the observations of the corresponding ICME at 1 AU (Section 5). We also summarize the main magnetospheric observations and supply detailed causal links between various magnetospheric phenomena and activities; in addition, we use the extrapolated magnetic field, speed, and ram pressure at 1 AU to get proxies of the magnetospheric response in terms of magnetospheric compression and Dst index (Section 6). We discuss our results and conclude the study in Section 7.

2. OVERVIEW OF THE ERUPTIVE FLARES OF 2012 MARCH 7

The source of the activity was NOAA AR 11429, hereafter 11429, with heliographic coordinates (N18, E31) and a $\beta\gamma\delta$ photospheric magnetic configuration on 2012 March 7 at 00:00:00 UT (Figure 3(b)). This AR was intensely eruptive and hosted several major events. The photospheric line-of-sight (LOS) HMI magnetogram of the AR (Figure 3(b)) shows a complex polarity inversion line (PIL) with strong fields and gradients. Strong shearing motions were also observed along the PIL (Chintzoglou et al. 2015). Flux-rope structures were detected in the overlying corona (Figure 3(c)) in the 94 and 131 Å AIA channels with peak temperature responses at ~ 6.4 and 10 MK, respectively (Lemen et al. 2012). The existence of pre-eruptive flux ropes was confirmed by the use of nonlinear force-free magnetic field extrapolations (Chintzoglou et al. 2015). Multiple flux ropes can result from the continuous emergence and reconnection of sheared field lines along the PIL in ARs undergoing dynamical emergence of weakly twisted flux tubes from the solar interior (Archontis et al. 2013, 2014). The pre-eruptive flux-rope structures were also observed in several other hot spectral lines (e.g., Ca xv ($\log T = 6.65$), Fe xxiii ($\log T = 7.15$), Fe xxiv ($\log T = 7.25$)) by the Extreme Ultraviolet Imaging Spectrometer (EIS; Culhane et al. 2007) onboard the *Hinode* mission (Kosugi et al. 2007). Using EIS spectroscopic observations, which offer much better temperature resolution than the AIA narrow-band images, Syntelis et al. (2015) showed that the flux-rope structures indeed contain hot (~ 6 –12 MK) plasmas.

The two flares occurred on 2012 March 7 (panel (B) of Figure 1). The first one was a *GOES* X5.4 flare with onset and peak times at 00:02 UT and 00:24 UT respectively. The flare originated from the eastern part of 11429 at heliographic coordinates (N18, E31). The second flare was a *GOES* X1.3 with onset and peak times of 01:05 UT and 01:14 UT, respectively. It originated from the western part of 11429 at heliographic coordinates (N15, E26). The two flares were associated with two ultra-fast CMEs launched from 11429. The CME associated with the first flare, hereafter CME1, was directed along the NE (Figure 3(d)). This can be seen from

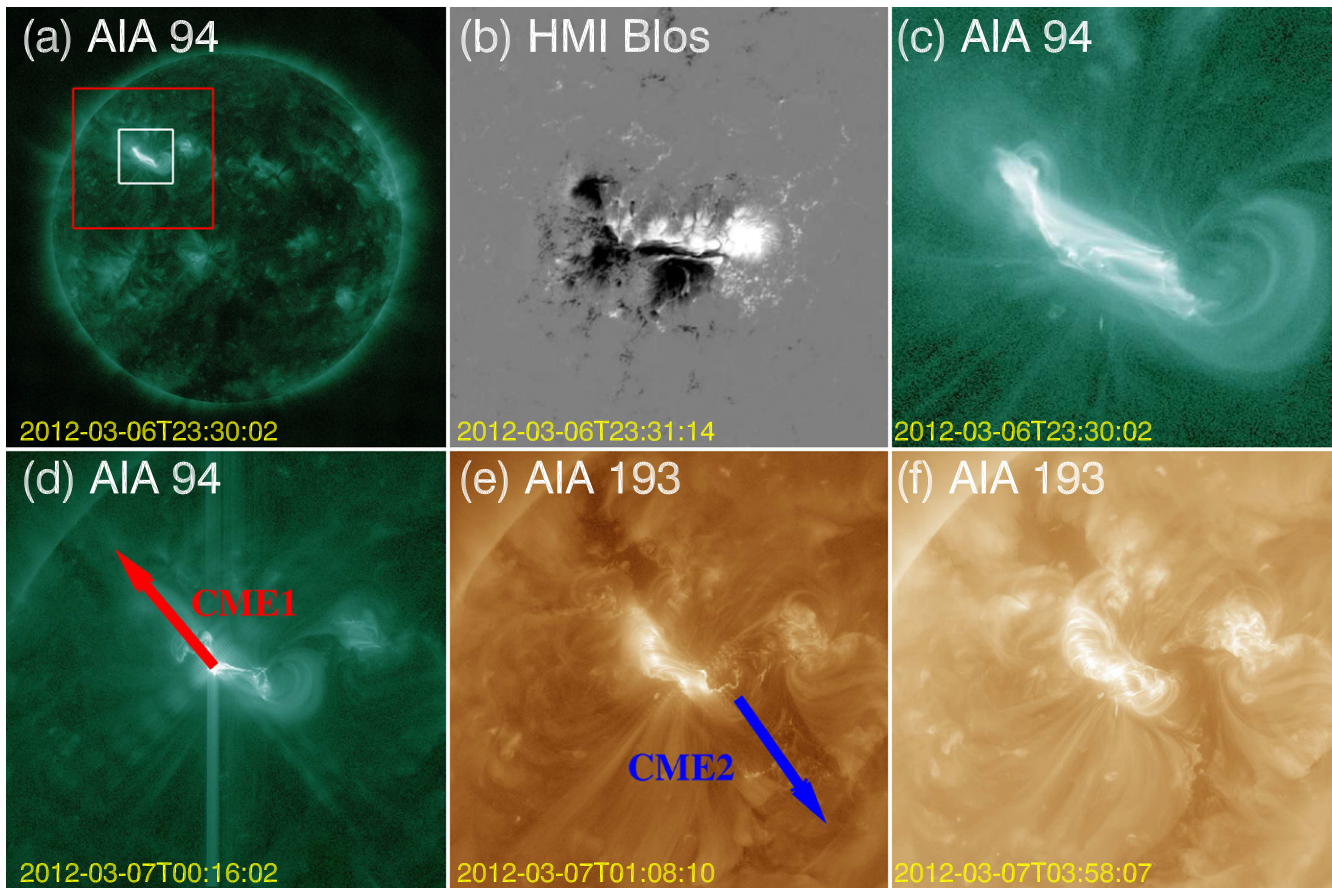


Figure 3. A description of the low-coronal configuration during the two eruptive X-class flares in NOAA AR 11429: (a) AIA 94 Å full-disk image less than an hour before the flares of 2012 March 7. The white box contains the source AR and is magnified in (b) and (c), while the red box contains a more extended field of view and is magnified in (d)–(f). The white and red boxes occupy areas of $300 \times 300 \text{ arcsec}^2$ and $780 \times 780 \text{ arcsec}^2$, respectively. The white box includes a photospheric line-of-sight HMI magnetogram (b) and the respective AIA 94 Å image (c). The red box includes a 94 Å AIA image obtained during the first flare (d), a 193 Å AIA image obtained during the second flare (e), and a 193 Å AIA image of the postflare phase (f). The inferred directions of the two corresponding CMEs in the inner corona, labeled here CME1 and CME2, respectively, are given by the red and blue arrows in (d) and (e), respectively.

(An animation of this figure is available.)

the corresponding ejecta (flux-rope structures and overlying loops) and associated dimmings in AIA movies (see online movie movie1.mp4 using AIA images from the 211 Å channel). The CME associated with the second flare, hereafter CME2, was directed along the SW (Figure 3(e) and online movie movie1.mp4). A post-eruption arcade surrounded by coronal dimmings was caused by the substantial CME-driven mass evacuation (Figure 3(f)). Linear fits of the height–time observations of CME1 and CME2 by *SOHO* LASCO C2/C3 from the Coordinated Data Analysis Workshops (Yashiro et al. 2004) gave speeds of ~ 2200 and 1800 km s^{-1} , respectively.

In summary, two ultra-fast CMEs in association with two powerful flares were launched from *different* parts of 11429 *within an hour* and propagated along *very different* directions in the inner corona.

3. CORONAL AND PHOTOSPHERIC OBSERVATIONS

Here we determine which CME, if not both, was Earth-directed, and estimate its helicity budget.

3.1. Geometrical Fitting of the Two CMEs

Finding which of the two CMEs—if not both—was Earth-directed is an important task since the CME that reached L1, almost two days later, triggered a major geomagnetic storm.

For this task the graduated cylinder shell (GCS) model of Thernisien et al. (2009) and Thernisien (2011) was used. This is essentially a geometric representation of a flux rope used to fit the CME envelope using simultaneous observations from two or three vantage points. The model depends on a number of free geometrical and positional parameters. The geometrical parameters are the flux-rope height h , angular width between the two legs $2w$, and aspect ratio k . The latter parameter determines the rate of expansion as a function of the CME height, so that the structure expands in a self-similar manner. The CME radius R at a heliocentric distance r is then

$$R(r) = kr. \quad (1)$$

The positional parameters determine the location and orientation of the flux rope. This is achieved by supplying the model's central heliographic (Stonyhurst) longitude ϕ and latitude θ as well as the orientation of its axis of symmetry (tilt) γ . The GCS

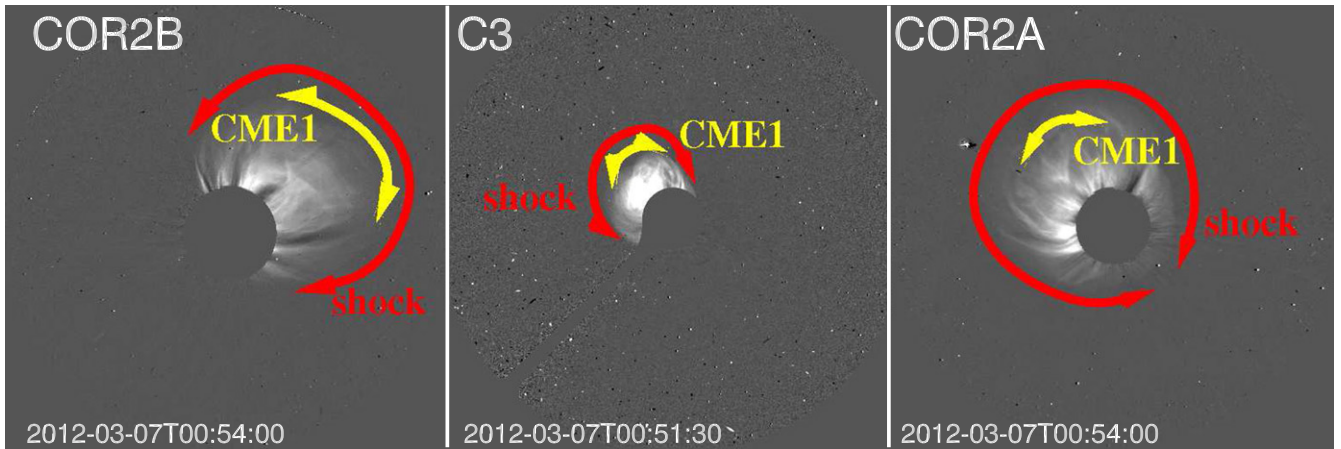


Figure 4. Triple-spacecraft views of CME1 and its associated shock as observed by COR2 on *STB* (left panel), C3 on *LASCO* (middle panel), and COR2 on *STA* (right panel). The yellow and red double arrows demarcate the extents of CME1 and shock1, respectively.

user varies these parameters on a trial-and-error basis until a good agreement is reached between the multi-viewpoint observations and the corresponding model projections.

*Triple-spacecraft white-light (WL) observations of CME1 and CME2 were used, involving simultaneous or nearly simultaneous observations from the COR2 coronagraphs of the SECCHI instrument suite and the LASCO C3 coronagraph. The COR2 field of view (FOV) is $2.5\text{--}15 R_{\odot}$ and that of C3 is $3.7\text{--}30 R_{\odot}$. On 2012 March 7 the *STEREO B* spacecraft (*STB*) was 110° behind Earth and the *STEREO A* spacecraft (*STA*) was 120° ahead (Figure 2). Given the location of 11429 and the separation between the *STEREO* spacecraft, CME1 and CME2 were approximately limb events for both *STA* (eastern limb) and *STB* (western limb). This symmetry introduces a degree of degeneracy in several parameters of the GCS model (most importantly the tilt angle). Therefore, using a “third” eye from the C3 observations was essential to guarantee an optimal fitting.*

Online movie movie2.mp4 shows the development of CME1 and CME2 in the coronagraphic observations. CME1 and CME2 entered the COR2/*STA* FOV at 00:39 UT and 01:39 UT on 2012 March 7, respectively. CME1 headed NE and CME2 headed SW. In tandem with CME1, an associated WL shock (hereafter shock1) was also observed. Shock1 was traced by faint propagating intensity fronts around CME1 and by deflected streamers (e.g., Vourlidas et al. 2003; Ontiveros & Vourlidas 2009). It was significantly broader than its driver, CME1, and practically encircled the occulting disk of the coronagraphs. This suggests that there had been an Earth-directed component of shock1. As a further illustration of the CME1–shock1 correspondence we demarcate the events’ spatial extent in Figure 4. Given the small spatio-temporal separation between the onsets of CME1 and CME2 the corona was significantly perturbed by shock1 and CME1 when CME2 was launched. This may have prevented the detection of a WL shock signature associated with CME2. It is very important not to confuse shock1 and CME2 with a possible Earth-directed component of CME1. Without a proper identification of the WL features in the coronagraph images one may be led to the erroneous conclusion that CME1 was Earth-directed. It was not. The analysis of shock1 and the corresponding SEP event can be found in Kouloumvakos et al. (2015). A major result of

this study is that the energetic protons detected at various locations in the heliosphere (e.g., L1, *STB*) were associated with shock1, in agreement with the study of Richardson et al. (2014).

The results of the triple-spacecraft fittings of CME1 and CME2 are shown in Figure 5 and the corresponding best-fit parameters can be found in Table 1. They correspond to the latest COR2B, C3, COR2A triplet for which it was possible to apply the GCS fitting to CME1 (upper row) and CME2 (lower row). Checking now the middle column in Figure 5 that contains the L1 (*SOHO*) fittings, it is obvious that CME2 was Earth-directed, heading toward the SW. CME1 must have clearly missed Earth given its NE heading. If CME2 propagated self-similarly, from the height range of our GCS fit to 1 AU, it would result in a flank impact by its western leg.

Several studies have dealt with the coronal and IP evolution of the ejecta associated with the 2012 March 7 events (Davies et al. 2013; Liu et al. 2013; Möstl et al. 2014; Rollett et al. 2014). All of them were largely based on time-elongation (jmap) measurements taken along the Sun–Earth line by the HI1 and HI2 heliospheric imagers of SECCHI. Note here that Davies et al. (2013), Liu et al. (2013), and Rollett et al. (2014) suggested that the Earth-directed CME was CME1. In contrast, Möstl et al. (2014) suggested that the Earth-directed CME was CME2. Since the outermost intensity front is typically tracked in jmaps, the above studies essentially tracked the shock/sheath region corresponding to shock1 and missed both CME1 and CME2.

Finally, an estimate of the length, L , of the CME2 front can be deduced. It is assumed that the CME2 front is a cylindrical section with an angular width given by the GCS fitting. Although it is obvious that the CME2 front is curved, we nonetheless consider a cylindrical shape for convenience. This is because (i) in Section 4.1 we will use a cylindrical model in our investigation of the CME2 magnetic field and (ii) CMEs may flatten during IP propagation (e.g., Savani et al. 2010). We can then write for L

$$L = 2wr_{\text{mid}}, \quad (2)$$

with r_{mid} being the heliocentric distance half-way through the model’s cross section along its axis of symmetry and w is given

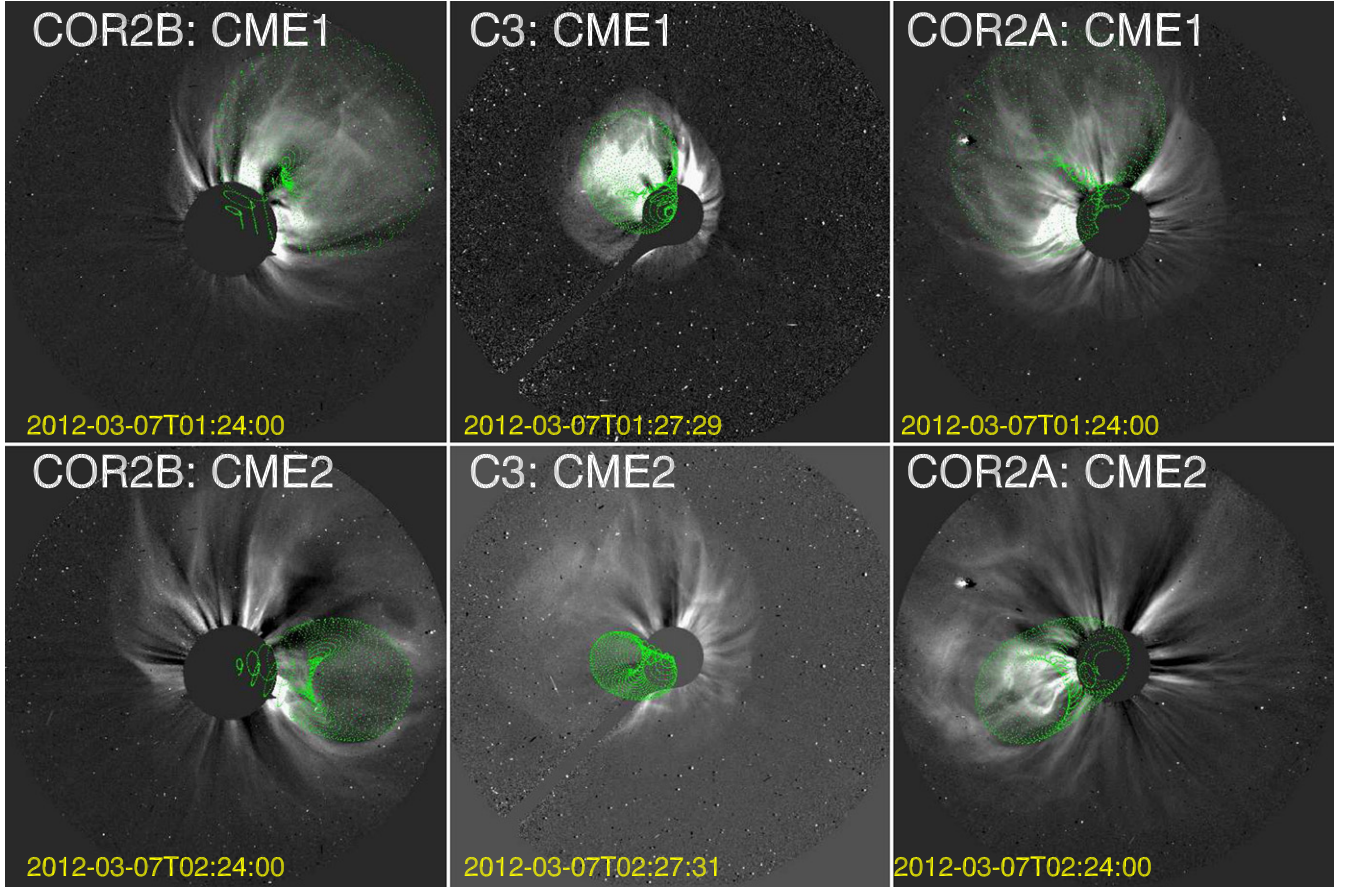


Figure 5. Triple-spacecraft GCS fittings (green wireframe) of CME1 (upper row) and CME2 (lower row). The first, second, and third columns contain COR2B, C3, and COR2A images, respectively.

(An animation of this figure is available.)

Table 1
Results of Triple-spacecraft GCS Fitting of the Two Analyzed CMEs

Event and Time	θ (deg)	ϕ (deg)	γ (deg)	H (R_{\odot})	κ	w (deg)
CME1 01:24 UT	323	31	-78	17	0.54	27.1
CME2 02:24 UT	320	-12.8	-33	13	0.36	23.47

Note. Shown are, from left to right, the event and corresponding UT on 2012 March 7, Stonyhurst longitude θ (deg) and latitude ϕ (deg), tilt angle γ (deg), CME height H (R_{\odot}), aspect ratio κ , and half-angle w (deg).

in radians. The corresponding CME2 cross-sectional area A is then

$$A = 2RL. \quad (3)$$

3.2. Estimating the Magnetic Helicity of CME2

In this section we present estimates of the magnetic helicity associated with CME2, using photospheric magnetic field observations. As we will see in full detail in Section 4.1, magnetic helicity enters into the calculation of the magnetic field of flux-rope CMEs. We follow three different approaches to estimate the relative magnetic helicity with respect to the current-free (potential) field. For brevity, we refer to relative magnetic helicity as magnetic helicity.

The first approach is the *helicity injection* method as implemented by Parlat et al. (2006), with the difference that the DAVE4M method (Schuck 2008) was used in the

determination of the photospheric horizontal flow vector. This method uses photospheric vector magnetograms to determine the photospheric horizontal flow vector and then calculates the proxy for helicity flux density G_{θ} , a quantity that eventually provides the instantaneous injection rate of magnetic helicity through the photospheric layer.

The second approach is the nonlinear force-free *magnetic-connectivity matrix* method of Georgoulis et al. (2012). This method also uses photospheric vector magnetograms and partitions the photospheric flux into elementary, slender flux tubes to calculate the magnetic helicity, both self and mutual, of the ensemble.

The third approach is a *nonlinear force-free volume* calculation of the magnetic helicity described in Moraitis et al. (2014). This method uses nonlinear force-free magnetic field extrapolations of the photospheric vector magnetic field into the corona and calculates the magnetic helicity in the

Table 2
Estimates of Magnetic Helicity Associated with CME2 from the Various Methods Used

Method of Calculation	Positive Helicity (Mx^2)	Negative Helicity (Mx^2)	Net helicity (Mx^2)
Helicity injection (Pariat et al. 2006)	7.87×10^{42}	-4.05×10^{43}	-3.26×10^{43}
Connectivity matrix (Georgoulis et al. 2012)	4×10^{42}	-8×10^{42}	-4×10^{42}
Volume calculation (Moraitis et al. 2014)	-8×10^{42}

extrapolated coronal volume. Notice that this method yields only the net helicity, while the first two methods can decompose the helicity into left-handed (i.e., negative) and right-handed (i.e., positive) helicity terms. Finally, it is important to realize that while the magnetic-connectivity and volume methods supply the instantaneous magnetic helicity, the helicity injection method supplies the helicity injection rate. K. Tziotziou et al. (2015, in preparation) provide a detailed description of the application of these methods to 11429.

The three methods were applied to the interval from 00:00 UT on 2012 March 6 to 00:00 UT on March 8. Time-series of HMI vector magnetograms covering the entire AR were used. We focus here on helicities calculated over the entire 11429 and determine changes in helicity budget before and after the onset of CME2, which is assumed to coincide with the onset of the associated X1.3 flare.

A summary of the helicity calculations pertinent to CME2 is given in Table 2. We note that all methods yield a net negative helicity. Significantly smaller changes in the positive helicity were also inferred by the helicity-injection and the connectivity-matrix methods. From Table 2 we also note that the higher helicity values correspond to the helicity injection method. However, the helicity budgets from this method do not represent instantaneous helicity budgets. This means that this method essentially provides the total helicity that was injected into the system from the beginning of the observing sequence until the onset of the corresponding eruption. Therefore, the helicity budget from this method should be considered as an *upper* limit on the helicity shed by CME2. On the other hand, the estimate of the connectivity-matrix method may be viewed as a lower limit on the helicity of CME2.

4. NEAR-SUN AND 1 AU MAGNETIC FIELD AND DYNAMICS OF THE EARTH-DIRECTED CME

This section describes a methodology used for the first time to infer the near-Sun magnetic field of flux-rope CMEs and to extrapolate it to 1 AU. In addition, we present a method to extrapolate the near-Sun kinematics of a CME to 1 AU. Both techniques are applied to CME2.

4.1. Estimating the Magnetic Field of the Earth-directed CME

Three simple analytical models of flux-rope CMEs are used, one force-free and two non-force-free, connecting the magnetic helicity and several geometrical properties of a CME to its magnetic field. We follow the work of Dasso et al. (2006), which provided analytical expressions for the magnetic helicity (H_m) of three cylindrical flux-rope configurations described in the Appendix.

Equations (A4), (A8), and (A11) of the Appendix give the CME axial magnetic field B_0 for the three models as a function of magnetic helicity (H_m) and geometrical parameters (flux-rope length L and radius R). B_0 is assumed to be constant along the major axis of the CME and we are dealing with a short

Table 3
Estimates of the Magnetic Field of CME2 at $13 R_\odot$

Method	B_0 (G)
Linear force-free (Lundquist 1950)	0.02–0.07
Non-force-free (Hidalgo et al. 2000)	0.05(0.01)–0.16(0.03)
Non-force-free (Cid et al. 2002)	0.04(0.01)–0.13(0.03)

Note. For the two non-force-free models the values outside and inside parentheses correspond to a total number of 0.5 and 10 turns, respectively.

section along the CME (i.e., omitting its full length and more specifically its legs). L and R were deduced in Section 3.1 from the geometrical modeling and H_m was deduced in Section 3.2 from the three different methods of magnetic helicity calculation. The twist parameter, τ_0 , in the two non-force-free formulations of B_0 (Equations (A8) and (A11)) is given by

$$\tau_0 = \frac{N_{\text{turns}}}{L}, \quad (4)$$

with N_{turns} the total number of field turns along the flux-rope axis. To estimate τ_0 we use L as calculated in Section 3.1 and assume that N_{turns} varies in the range [0.5, 10], corresponding to the extreme cases between a weakly and a strongly twisted (multi-turn) flux rope.

With all required parameters derived from observations, the geometrical fitting of CME2, and the magnetic helicity analysis, the magnetic field of CME2 at $13 R_\odot$ is determined, which is the maximum height of application of the GCS model. A total of 15 values of the magnetic field are calculated. They result from the use of the three helicity values of Table 2 in the three considered models (one force-free, two non-force-free with two different twist parameters). The results are shown in Table 3 and give magnetic fields in the range 0.01–0.16 G; the average value is 0.05 G. There are few observational studies of the coronal magnetic field at $13 R_\odot$. They rely on techniques such as Faraday rotation and CME–shock stand-off distance and give magnetic field strengths in the range 0.009–0.02 G (e.g., Bemporad & Mancuso 2010; Gopalswamy & Yashiro 2011; Kim et al. 2012; Poomvises et al. 2012; Mancuso & Garzelli 2013). Ours is the first attempt to obtain the CME-entrained field at those heights, however. Our estimates exceed the past estimates of the background magnetic field by 8–17 times. This is consistent with the established notion of CMEs as magnetic flux ropes (MFRs) and hence objects of enhanced magnetic field relative to the background corona. However, further studies on a larger sample of events would be very helpful in determining whether our current methodology is reliable enough to estimate CME magnetic fields in the corona.

Before completing this part of the analysis, we comment on the basic assumptions of our methodology. First, a flux-rope CME was assumed. Most CMEs exhibit a flux-rope morphology at coronagraphic heights (Vourlidas et al. 2013). This clearly seems to be the case for CME2 (Figure 5), which displays the familiar three-part structure in its limb views. In

addition, CME2 is described well by a simple geometrical flux-rope model (see Section 3.1). Second, the utilized helicity values resulted from calculations pertinent to the photosphere/low corona and not to the outer corona, where the CME geometrical fitting took place. However, this can be justified by the conservation property of magnetic helicity even in the presence of magnetic reconnection (e.g., Berger 1984). If the detected helicity change in the photosphere/low corona fueled CME2 in its entirety, then it should be conserved for a plasma of low β and high Reynolds number, which is reasonably true up to $13 R_\odot$. Third, in addition to a force-free flux-rope model, non-force-free flux-rope models are also used to account for possible departures of CMEs from force-freeness (e.g., Subramanian et al. 2014). Fourth, the assumption was made that the GCS-fitted CME radius is equal to the corresponding flux-rope radius. This essentially equates the radius of the observed CME cavity to the radius of a flux rope. Multi-temperature extreme UV observations monitoring CME initiation in the low corona show that sometimes the flux rope fills only a fraction of the available cavity volume (e.g., Zhang et al. 2012; Patsourakos et al. 2013; Kliem et al. 2014). However, in the course of time the flux rope progressively fills in the cavity, possibly via the reverse pinch effect (Kliem et al. 2014). Therefore, at coronagraphic heights the CME cavity should be fully covered by the flux rope (see, for example, Figure 5 in Vourlidis et al. 2013).

4.2. Extrapolating the Magnetic Field of the Earth-directed CME to 1 AU

To extrapolate the magnetic field magnitude of CME2 from $13 R_\odot$ to 1 AU we assume that it is described by a power law of the heliocentric distance r ,

$$B_0(r) = B_*(r/r_*)^{\alpha_B}, \quad (5)$$

with B_* corresponding to the magnetic field of the CME at some reference distance r_* and α_B the power-law index. For α_B we consider values in the range $[-2.7, -1.0]$, with a step of 0.1. This range results from various mainly observational, as well as theoretical, studies covering either the outer corona or the inner heliosphere or, a few times, both (e.g., Patzold et al. 1987; Kumar & Rust 1996; Bothmer & Schwenn 1998; Vršnak et al. 2004; Liu et al. 2005; Forsyth et al. 2006; Leitner et al. 2007; Démoulin & Dasso 2009; Poomvises et al. 2012; Mancuso & Garzelli 2013). When applying Equation (5), B_* was taken equal to the values corresponding to the minimum, average, and maximum of the distribution calculated at $r_* = 13 R_\odot$ (Table 3). The resulting magnetic field of CME2 at 1 AU ($r = 215 R_\odot$) has values in the range $[0.55, 1002.2]$ nT, its median value being 26.5 nT. Figure 6 contains the extrapolated values of B_0 at 1 AU as a function of α_B . Steep radial fall-offs of B_0 (i.e., $\alpha_B \approx -2.0$) of the ICME magnetic field are broadly consistent with the range of the associated ICME magnetic field values observed in situ at 1 AU. On the other hand, shallower radial fall-offs of B_0 (i.e., smaller absolute α_B) give rise to significantly higher ICME magnetic fields that appear inconsistent with the observations albeit within large uncertainties. We finally anticipate that the CME–ICME magnetic field could vary faster with r closer to than further away from the Sun. Thus a single power-law description of $B_0(r)$ is possibly only an approximation. Using

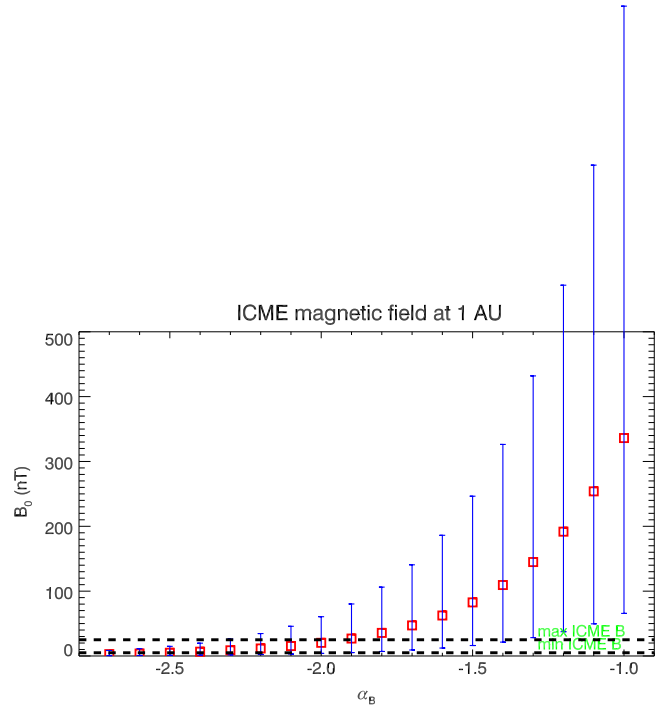


Figure 6. Extrapolated CME2 magnetic field at 1 AU as a function of the radial power-law index α_B of the magnetic field magnitude (Equation (5)). The squares, lower, and upper error bars correspond to the average, minimum, and maximum values of the CME magnetic field calculated at $13 R_\odot$, respectively (see Section 4 and Table 3). The lower and upper horizontal lines correspond to the minimum and maximum magnetic field magnitude of the associated ICME as deduced from the in situ *Wind* observations presented in Section 5.

two power laws (not shown here)—a steep one from $13 R_\odot$ to 0.3 AU (i.e., the perihelion distance of the *Helios* observations corresponding to several of the α_B determinations discussed above) connected with a shallower one from 0.3 to 1 AU—showed again that steep radial fall-offs are required to match the ICME magnetic field at 1 AU.

4.3. Extrapolating the Kinematics of the Earth-directed CME to 1 AU

To extrapolate the kinematics of CME2 to 1 AU the standard aerodynamic drag-force model approach is used (see for example Cargill 2004; Byrne et al. 2010; Vršnak et al. 2010). The aerodynamic drag force F_D is written as

$$F_D = C_D M_{\text{CME}} \rho_w C_D A (v_{\text{CME}} - v_w) |v_{\text{CME}} - v_w|, \quad (6)$$

with C_D a dimensionless drag-force coefficient, M_{CME} the CME mass, ρ_w and v_w the upstream mass density and speed of the solar wind, respectively, v_{CME} the CME speed, and A the CME cross-sectional area. Equation (6) is solved by numerical integration from a starting height of typically $20\text{--}30 R_\odot$ (e.g., Vršnak et al. 2010), where the drag force is assumed to dominate the CME dynamics.

For M_{CME} a COR2B mass image was used because CME2 was very close to the *STB* plane of the sky according to the GCS modeling. CMEs tend to reach their final mass at around $10 R_\odot$ (e.g., Vourlidis et al. 2010). The mass calculation was performed over the upper section of CME2 and did not include its legs, as mentioned before. This is because the drag force on a CME is mainly relevant to its upper section, which is

perpendicular to a radial solar wind flow, and not to its legs, which form much smaller angles with respect to the wind. A was determined from Equation (3). For C_D we made the usual assumption that it does not vary strongly with the radial distance and assumed it equal to 1 (e.g., Cargill 2004).

In most applications of the drag-force model, v_w and ρ_w profiles correspond to quiescent solar-wind conditions. Here we use the electron density profile of Leblanc et al. (1998) normalized to the density observed in situ at 1 AU two days before the arrival of CME2. The solar wind speed profile resulted from mass conservation.

However, we suspect that CME2 did not encounter quiescent upstream solar wind in its transit to 1 AU. This is because of the shock associated with CME1 (shock1), which had an Earth-directed component and possibly previous solar activity. To better account for the disturbed inner heliosphere and to construct more reliable v_{CME} and ρ_w profiles, an MHD simulation of shock1 was performed. For this task we used the ENLIL code (Odstrčil & Pizzo 1999, 2009), based at the NASA Community Coordinated Modeling Center (CCMC; run Spiros_Patsourakos_020314_SH_1). ENLIL is a time-dependent 3D MHD model of the heliosphere. A heliospheric disturbance, i.e., a hydrodynamic structure with enhanced density (thus pressure) and velocity, is applied to ENLIL's inner boundary at $20 R_\odot$. The 3D time-dependent MHD equations are solved in the domain $20 R_\odot$ – 2.0 AU, 60° north to 60° south in latitude and 360° in azimuth. A steady heliospheric solution is used as the initial condition. The applied disturbance is meant to crudely approximate shock1 in the inner boundary of ENLIL. Several parameters of the disturbance were constrained by the geometrical fitting of shock1, described in full by Kouloumvakos et al. (2015). In a nutshell, a spheroid model was used to fit the envelope of shock1 in COR2B/C3/COR2A triplets analogously to the CME fittings of Section 3.1. The fitting provided shock1's central longitude and latitude, angular width, and speed at $20 R_\odot$.

The model results were validated by comparing the simulated time-series of solar wind speed and density at 1 AU to *Wind* in situ measurements (Figure 7) with encouraging results. First, the shock arrival time predicted by the ENLIL simulation lags the *Wind* observations by about 60 minutes.¹³ Second, the predicted shock-front speed is almost equal to the speed in the *Wind* observations while the density is overestimated by a factor of almost 2. The latter is possibly a consequence of specifying a homogeneous density for the heliospheric disturbance. Therefore, the ram pressure jump ($\propto \rho v^2$) is overestimated by a similar factor (bottom panel in Figure 7). Third, there is a qualitatively similar behavior in the simulated and observed solar wind time-series both before and after the shock arrival. Therefore, the MHD modeling captures the essential properties of the observed shock at 1 AU.

We can now extract the radial profiles of solar wind density and speed of the pressure pulse from $30 R_\odot$ to 1 AU. Using radial rather than temporal (Lagrangian) profiles of these quantities mitigates the small temporal offset between the simulated and observed shock. The radial profiles are extracted along the direction of CME2 propagation as determined by the geometrical fitting at $13 R_\odot$.

¹³ Numerical diffusion broadens shocks, and thus taking the middle of the leading slope of the simulated shock of Figure 7 as a proxy of its arrival time at 1 AU is a reasonable assumption.

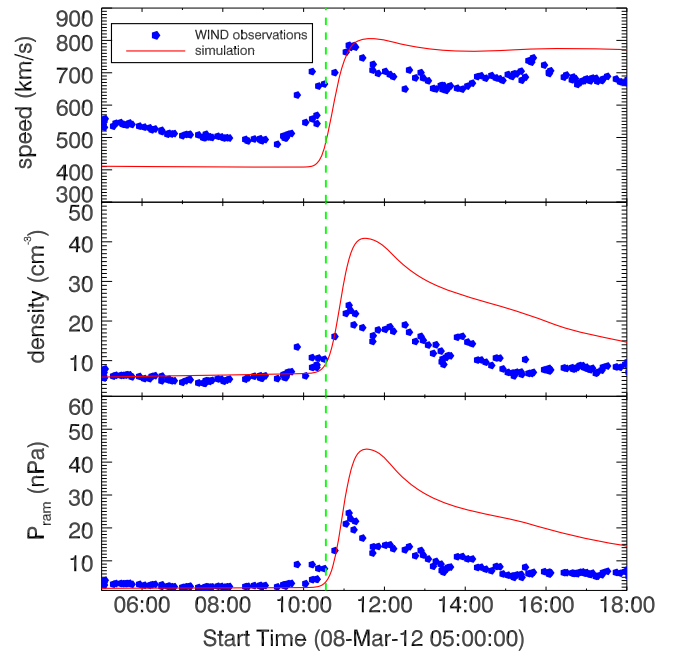


Figure 7. Solar wind speed (top), density (middle), and ram pressure (bottom) at 1 AU from in situ *Wind* observations (blue dots) and from the ENLIL simulation (red curve). The vertical green dashed line marks the shock arrival at 1 AU.

Finally, the CME2 speed at $30 R_\odot$ was determined by extending the GCS fitting to the FOV covered by the SECCHI-A and -B H11 imagers. Given that CME2 was a limb event for both spacecraft, the corresponding H11 views were not able to fully constrain the CME2 fitting. We thus fixed all the parameters of the modeling in the H11 FOV from our COR2 (STA/STB) and C3 modeling of Section 3.1 and varied only the height (see also Colaninno et al. 2013). A linear fit of the resulting height–time measurements in the range 20 – $30 R_\odot$ gave a speed of $\sim 1500 \text{ km s}^{-1}$ at $30 R_\odot$.

Figure 8 shows the temporal evolution of the CME2 speed from $30 R_\odot$ to 1 AU, based on Equation (6) subject to either quiescent (red curve) or perturbed (green curve) upstream solar-wind conditions. Assuming quiescent upstream conditions results in a strong CME2 deceleration, delaying its 1 AU arrival by ~ 8 hr. In addition, the predicted CME2 speed at 1 AU is almost 100 km s^{-1} slower than the observed one. Using the perturbed conditions derived from the ENLIL model improves predictions considerably. The predicted CME2 arrival at 1 AU is only 2 hr later than the observed arrival time, while its predicted speed differs by only $\sim 10 \text{ km s}^{-1}$ from the observed one. The relative success of the model using perturbed upstream solar-wind conditions in predicting the 1 AU transit time and speed of CME2 is because of the elevated (with respect to a quiet solar wind) upstream solar wind. This essentially reduces the CME deceleration that tries to adjust its speed to a faster background, resulting in an earlier CME arrival. This is a further validation of our modeled upstream solar wind and further emphasizes the need for proper background-wind measurements for improved CME kinematics studies.

5. ICME OBSERVATIONS AT 1 AU

We now move to the analysis of the in situ observations of CME2 and related phenomena observed at L1. In situ magnetic

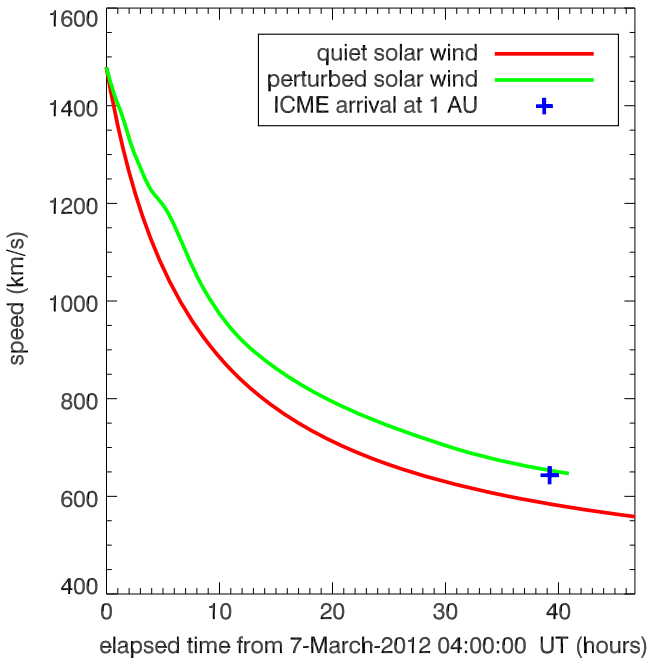


Figure 8. Temporal evolution of CME2 velocity from $30 R_{\odot}$ to 1 AU as determined from the application of the drag-force model for quiet solar wind (red curve) and perturbed solar wind (green curve). Each curve terminates when the modeled CME reaches 1 AU. The blue cross designates the actual arrival time and speed of ICME2 as deduced from in situ *Wind* observations.

field and plasma measurements from the *Wind* spacecraft are used. These measurements are shown in Figure 9. A first remark immediately drawn from Figure 9 is that the IP medium was significantly perturbed and contained several complex structures (ICMEs, shocks, and sheaths). During day 67 (2012 March 7) a shock followed by an ICME-like structure reached L1. These disturbances were related to a CME launched from 11429 on 2012 March 5 (e.g., Magdalenic et al. 2014). On 2012 March 8 (day 68) at around 10:30 UT, jumps in all displayed solar wind parameters were observed, signalling the arrival of shock1 at L1 (Section 4.3). The shock is followed by a sheath region characterized by significant fluctuations in all related physical parameters (e.g., Malandraki et al. 2005).

Around 19:15 UT on 2012 March 8, an ICME presumably corresponding to CME2 reached 1 AU. Its arrival gave rise to a period of enhanced magnetic field, low plasma density and temperature, proton- β plasma parameter less than 1, and bi-directional electrons (bottom panel of Figure 9). All these are key properties of ICMEs (e.g., Burlaga et al. 1981). Around 6 hr after the ICME arrival at L1, magnetic field components exhibited significant rotation (B_z turned from northward to southward). This is an indication that the CME may have contained a magnetic cloud (MC) structure (e.g., Burlaga et al. 1981). However, during this period of rotation, the magnetic field magnitude exhibited a strong “negative” spike, in the form of an abrupt decrease, while the proton density, temperature, and proton- β plasma parameter (its values, nonetheless, remaining below 1) exhibited abrupt increases. The observed spikes may be suggestive of reconnection taking place in the interior of the ICME (e.g., Gosling et al. 2007). The presence of these spikes complicated significantly the interpretation and modeling of the ICME structure. After rotating, the magnetic field evolved in a much smoother fashion. The CME passage ended around 12 UT on March 11

(day 71) as *Wind* entered a region with proton- β plasma parameter higher than 1. All these findings suggest a rather complex and composite ICME structure, remote from the much simpler, “textbook-case” ICMEs and MCs.

The MC model of Nieves-Chinchilla et al. (2015) was applied to the *Wind* magnetic field observations. This model is based on the non-force-free concept developed by Hidalgo et al. (2002) and generalized in terms of the radial dependence of the poloidal and axial current density components. In fitting the observed magnetic field components, the model makes no assumption about the force distribution, thus allowing for departures from force-freeness, and it solves the Maxwell equations in circular-cylindrical coordinates.

The model was applied to three representative intervals (in fractional days counting from the beginning of 2012): (1) 68.89–69.43, covering the interval of strong magnetic field rotation and the magnetic field spike; (2) 69.09–70.35, corresponding to a period starting just after the end of the magnetic field spike; (3) 69.53–70.14, corresponding to a period of smooth variation of the magnetic field. These fittings gave rise to significantly different parameters. For example, the resulting MC-axis orientations had a maximum difference of $\sim 74^\circ$ among the different employed intervals. This result highlights the complex conditions at L1 that prevented us from further exploitation of the in situ data and from drawing further connections between the coronal and the in situ observations (e.g., in determining the rotation of the CME axis from the Sun to 1 AU).

We finally note that the *Messenger* spacecraft (Solomon et al. 2001) orbiting Mercury at a heliocentric distance of ~ 0.31 AU at $\sim 60^\circ$ east of the Sun–Earth line (left panel of Figure 2) observed a *single* ICME structure during early 2012 March 7. This is indirect evidence of a single Earth-directed CME (CME2). Had there been two CME structures traveling toward Earth, their corresponding signatures would most likely have not been entirely washed out so close to the Sun.

6. MAGNETOSPHERIC RESPONSE

In this section we overview the wealth of magnetospheric observations associated with the solar activity described above and offer detailed causal links and associations between the diverse observed phenomena. A full description will be given in T. Sarris et al. (2015, in preparation). In addition, we use several parameters of CME2 and shock1 at 1 AU, as determined in the previous sections to make some rough predictions of the corresponding magnetospheric response in terms of magnetospheric compression (Section 6.1) and Dst index (Section 6.2). Figure 10 describes the basic steps of the models predicting the magnetospheric compression (right-hand column) and the Dst index (left-hand column), which are described in detail in Sections 6.1 and 6.2, respectively.

6.1. Magnetospheric Compression

The arrival at L1 of the pressure pulse associated with shock1 resulted in a particularly strong compression of the magnetosphere. The *THEMIS* A, D, and E spacecraft were inside the magnetosphere before the pressure pulse arrival at L1¹⁴ and shifted into the magnetosheath as a result of the shock arrival and magnetospheric compression.

¹⁴ *THEMIS* A and D were very close to *THEMIS* E and observed similar features.

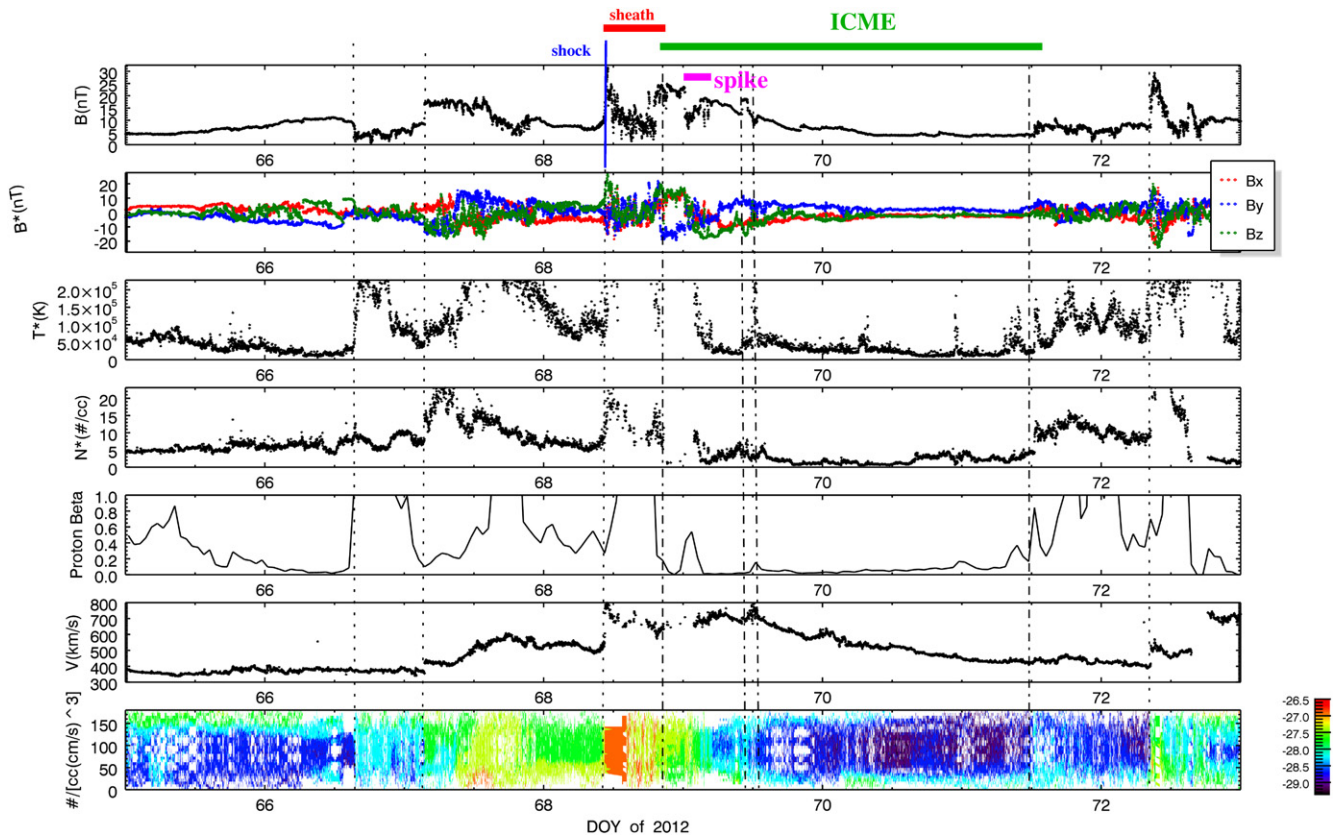


Figure 9. Wind L1 in situ observations (from top to bottom): magnetic field magnitude, magnetic field components in the GSE system; proton temperature; proton density; proton plasma β ; solar wind bulk velocity; pitch-angle distribution of energetic electrons at various energy levels. The vertical blue line marks the shock arrival, the red horizontal bar the associated sheath region, the green horizontal bar the ICME structure, and the magenta horizontal bar the magnetic field spike (all in top plot).

THEMIS E observations are summarized in Figure 11. Just prior to arrival of the pressure pulse at around 10:30 UT on March 8, the *THEMIS E* satellite was inside the magnetosphere at an average location of $[-2, -9.5, 4]$ Earth radii (R_E) in GSE coordinates. As can be seen from plots (a)–(e), upon the impact of the CME shock on the terrestrial bow shock, the plasma and magnetic field behavior changed dramatically as the spacecraft traversed the magnetopause and entered the magnetosheath. The entry into the magnetosheath was accompanied by a strong increase in the plasma density by an order of magnitude (Figure 11(a)) and a simultaneous increase in plasma velocity both earthward and downward, with V_x and V_y reaching values of $\sim -600 \text{ km s}^{-1}$ and $\sim -300 \text{ km s}^{-1}$, respectively (Figures 11(b) and (c)). The latter demonstrates clearly the deflection of the shocked solar wind plasma around the magnetosphere due to its impingement on the magnetopause. Due to the pressure pulse of the IP shock, the magnetic field inside the magnetosheath was highly compressed and turbulent and had a higher value than the magnetospheric one (Figure 11(d)). This runs counter to the typical situation (Phan et al. 1994). As has been shown and proposed by previous studies (Grib & Martynov 1977; Grib et al. 1979), the impact of a fast shock on the magnetopause produces a fast rarefaction wave moving sunward. This reflected rarefaction wave initiates an oscillatory process in which other secondary waves are generated by the reflections on both the bow shock and the magnetopause. This mechanism is responsible for producing oscillations of the magnetopause and bow-shock positions. Indeed, this oscillatory magnetopause behavior is demonstrated in

Figures 11(a) and (e), where very brief magnetopause crossings are clearly seen in both the plasma density and the electron plasma distribution (vertical red dotted lines). In summary, due to the global shrinkage of the magnetosphere caused by the arrival of the IP shock, *THEMIS E* spacecraft entered the magnetosheath and encountered a colder and denser plasma (Figures 11(e) and (a)), and remained there for ~ 10.5 hr until $\sim 21:30$ UT (second vertical black dotted line).

To predict the magnetospheric compression due to the arrival of shock1 at L1 the model of Tsyganenko & Sitnov (2005; TS05 hereafter) was used. In a nutshell, TS05 is a physics-based empirical model of the magnetosphere and takes as inputs the solar-wind dynamic pressure, the Dst index, and the IMF components perpendicular to the Sun–Earth direction. This model pertains to calculations of “active” internals, i.e., substorm and storm dynamics. The shock1-associated jump in the dynamic pressure from the ENLIL simulations (Section 4.3) is used in the modeling. The remaining parameters were extracted from the NOAA-SEC database. The various steps of the magnetospheric-compression prediction model are summarized in the right-hand column of Figure 10. We find that the magnetospheric compression and the location of the magnetopause nose have a stronger dependence on the solar-wind dynamic pressure than the Dst index and the IMF components perpendicular to the Sun–Earth direction.

Three representative snapshots during 2012 March 8 were considered: one at 07:55 UT, before the arrival of the pressure pulse at L1, one at 12:00 UT, shortly after its arrival and close to its peak (Figure 7), and one at 16:05 UT, during

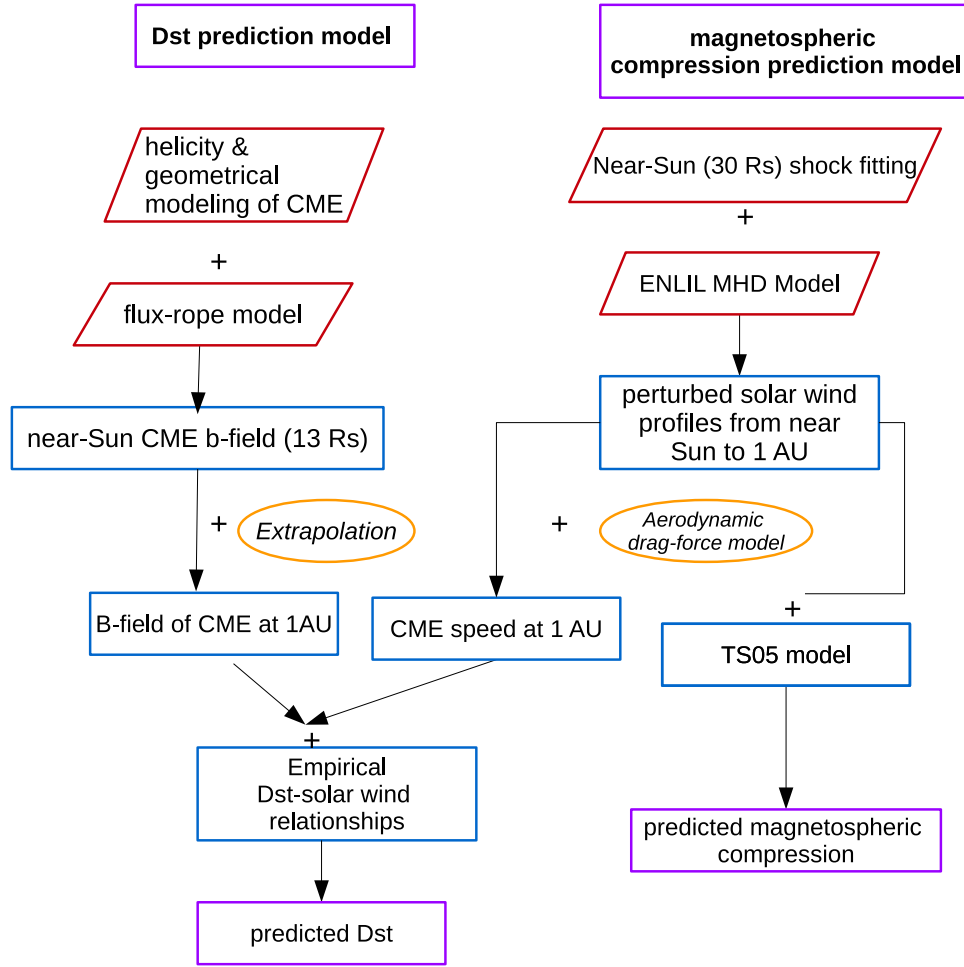


Figure 10. Flowchart showing our models for predicting the minimum Dst index (left-hand column) and the magnetospheric compression (right-hand column). Rhomboids and ovals correspond to methods and calculations while boxes correspond to results.

the decay phase of the pulse. Thus the first snapshot corresponded to a “quiet” magnetosphere, the second to a period of strong compression, and the third to a period of weaker compression.

The results of our modeling are shown in Figure 12. A significant shrinkage and earthward shift of the magnetopause can be seen after the arrival of the pressure pulse. For example, the magnetopause nose moves earthward by $\approx 3 R_E$ by 12:00 UT. The magnetospheric compression shifted *THEMIS* A, D, and E, which were initially inside the magnetosphere (first panel of the second row of Figure 12), to the magnetosheath after the arrival of the pressure pulse (second and third panels of the second row of Figure 12). Therefore, our results are in qualitative agreement with observations by *THEMIS* that indicate the entry of *THEMIS* E into the magnetosheath following the arrival of the pressure pulse. Tsironis et al. (2015) used the outputs of various Tsyganenko models to trace test particles and determine the resulting ring-current dynamics as well as to assess the various contributions to the resulting Dst index.

6.2. Geomagnetic Storm

Figure 1 provides a clear timeline of the geomagnetic response to the events of early 2012 March 7. The arrival of the strong pressure pulse at 1 AU around 10:30 UT on 2012

March 8 marks a particularly pronounced SSC with the Dst index attaining high positive values of ~ 50 nT. The southward magnetic field in the sheath region drives a decrease in the Dst index to ~ -30 nT. The main phase of the storm starts when the ICME magnetic field becomes southward, after an initial interval of northward magnetic field. The Dst index reaches a peak of ~ -148 nT at around 12 UT on 2012 March 9, at the maximum magnitude of the southward ICME magnetic field. The recovery phase of the storm lasted for ~ 2 days.

To connect the estimates of the CME2 magnetic field and speed at 1 AU (Sections 4.2 and 4.3) with its geomagnetic impact in terms of the Dst index, the empirical relationships in Wu & Lepping (2005) are used. These authors found that the upstream solar wind speed (V) and the magnitude of the southward magnetic field (B_z) of 135 MCs observed in situ are correlated with the minimum Dst index (Dst_{\min}) of the associated geomagnetic storms as

$$Dst_{\min} = 0.83 - 7.85 \times B_z, \quad (7)$$

and

$$Dst_{\min} = -16.48 - 12.89 \times (VB_z). \quad (8)$$

Although more accurate empirical relationships exist (e.g., Temerin & Li 2006), it is unnecessary to use them given the

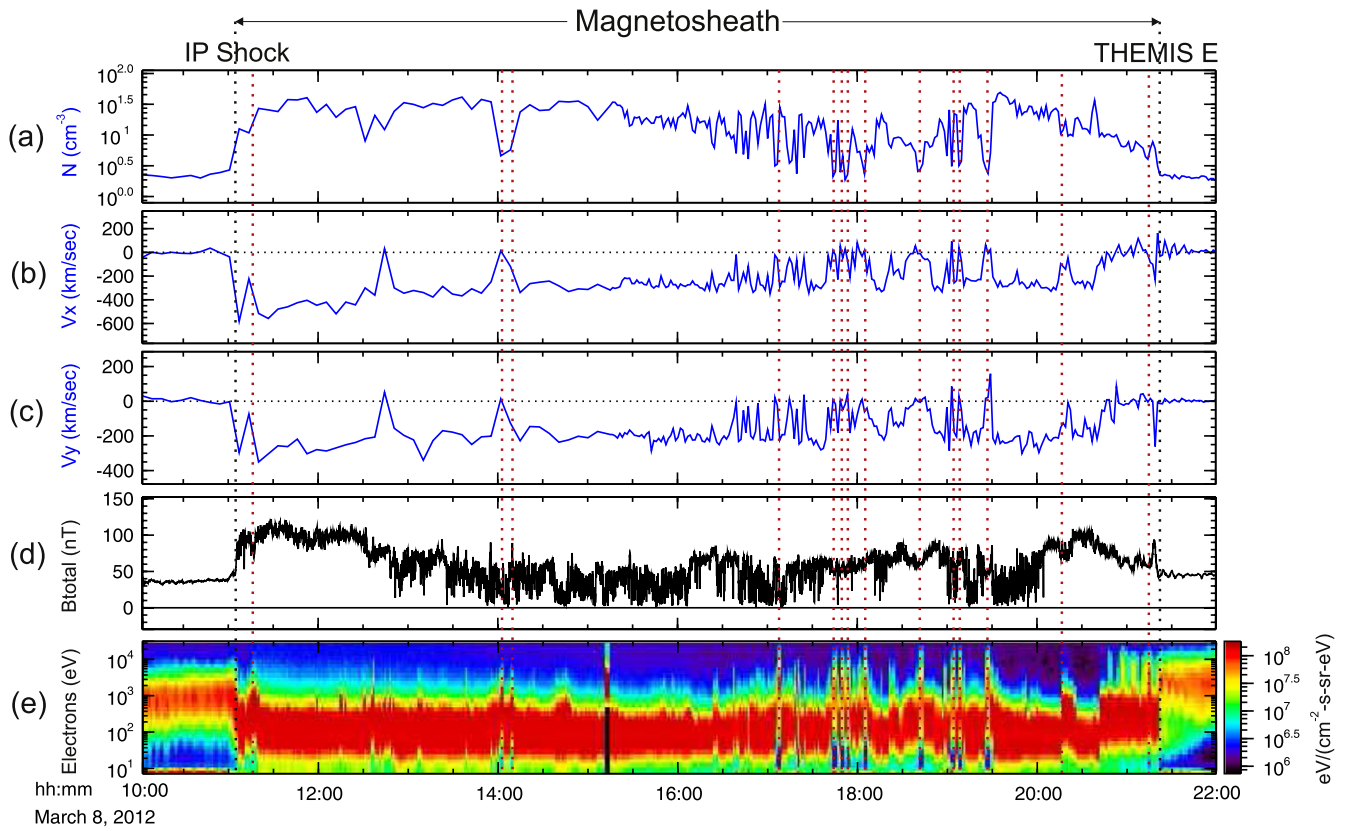


Figure 11. *THEMIS E* observations during 2012 March 8. Plots from top to bottom contain time-series of: (a) plasma density measured from the Electro-Static Analyzer (ESA; McFadden et al. 2008) instrument, (b), (c) the x and y components of the plasma flow velocity in geocentric solar magnetospheric (GSM) coordinates measured also from the ESA instrument, (d) the magnetic field strength B_{total} measured from the FGM (Flux/Gate Magnetometer; Auster et al. 2008) instrument, and (e) ESA electron plasma distribution. The vertical red dashed lines denote clear magnetopause crossings due to the oscillatory motion of the magnetopause, while the black dashed lines mark *THEMIS E*'s initial entry to and final exit from the magnetosheath. Similar observational features were also registered from *THEMIS A* and *D* (not shown here).

uncertainty of the extrapolated CME2 parameters at 1 AU. To calculate B_z , we use the extrapolated magnetic field magnitude of CME2 at 1 AU and account for the full-width-at-half-maximum range of the axis inclinations of ICMEs with respect to the ecliptic plane ($\approx 50^\circ$). The latter was deduced from the fitting of the in situ observations of 46 MCs described in Bothmer & Schwenn (1998). V was taken from the calculations of Section 4.3. The various steps in modeling the Dst index prediction are summarized in the left-hand column of Figure 10.

The resulting Dst_{min} is plotted as a function of the radial power-law index α_B of the CME magnetic field magnitude (Equation (5)) in Figure 13. For a given α_B and empirical Dst_{min} relationship (Equations (7) and (8)) Dst_{min} is estimated from the extrapolated to 1 AU magnetic field values corresponding to the average value of the CME2 magnetic field at $13 R_\odot$ (see Table 3 and Section 4.1) and solar-wind velocity V from Section 4.3.

The predicted Dst_{min} lies close to the observed Dst_{min} for α_B varying within a narrow interval around -2.0 and deviates significantly otherwise. The comparison between the predicted and the actual Dst_{min} is adequate, given uncertainties in B_z prediction and the exploratory scope of the investigation. It is hoped that application to simpler events should result in tighter constraints on such determinations.

6.3. Substorm Activity

Significant substorm activity was detected in geosynchronous equatorial orbit (GEO) by *GOES*-13 and 15 during the studied major geomagnetic storm. From Figure 14(a) five electron injection events, tagged with A, B, C, D, and E, can be discerned in the interval 00:00–18:00 on 2012 March 9. They are manifested as strong enhancements by almost two orders of magnitude in the differential electron fluxes at 275 keV. They occurred during the main phase of the associated geomagnetic storm, when a strong southward B_z of the IMF was observed (Figure 1). The injection events are directly related to abrupt or gradual changes in the AL index profile for the same interval (Figure 14(b)), which measures perturbations of the Earth's magnetic field over the Northern Hemisphere auroral zone. The five injection events (i.e., substorms) resulted in exceptionally high AL values from -1500 to -2500 nT. Given that at the end of each substorm the energetic-electron fluxes were higher than the pre-storm values, it is concluded that an acceleration process was at work (e.g., see the discussion in Sarafopoulos et al. 2001).

The abrupt decrease of the AL index at $\sim 11:30$ UT signifies the occurrence of an intense, distinct magnetospheric substorm. Almost at the same time, *GOES*-13 records the injection of plasma and energetic particles. Around ~ 9 minutes later, *THEMIS B* and *C*, positioned in the distant magnetotail, record a well-structured MFR with similar features. This entity is formed somewhere near Earth and propagated tailward. Given that *THEMIS B* is located at $(X, Y, Z)_{\text{GSE}} = (-57.67, -13.86,$

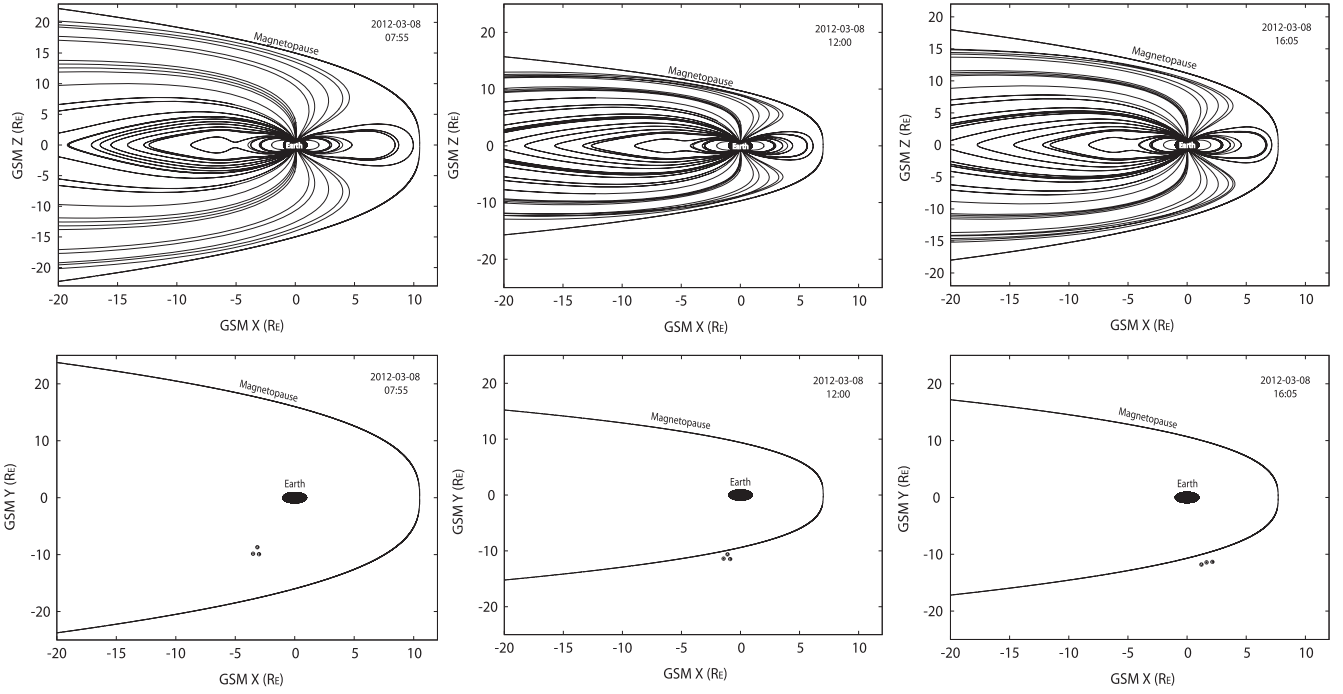


Figure 12. Simulations of the magnetosphere using the TS05 model before and after the arrival of the pressure pulse at L1. The first row contains representative field lines and the magnetopause projected on the X - Z plane of the GSM system while the second row contains the projection of the magnetopause and of the locations (displayed with small circles) of *THEMIS* A, D, E spacecraft on the GSM X - Y plane (the positions of the *THEMIS* spacecraft were too close to Earth on the GSM X - Z plane to be displayed with clarity). The first column contains a snapshot before the arrival of the pressure pulse at 07:55 UT on 2012 March 8, and the second and third columns correspond to 12:00 UT and 16:05 UT on 2012 March 8, respectively. The latter snapshots correspond to instances shortly after and well after the arrival of the pressure pulse at 1 AU.

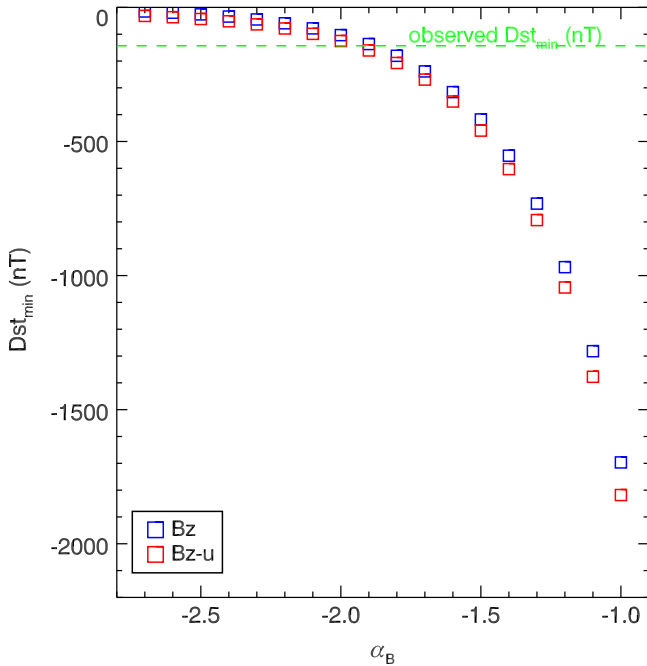


Figure 13. Predicted Dst_{\min} values from the extrapolated CME2 magnetic field and velocity at 1 AU, including also empirical relationships connecting Dst and solar-wind properties. Predicted values are plotted as a function of the radial power-law index α_B of the ICME magnetic field magnitude (Equation (5)), estimated from the average magnetic field of CME2 at $13 R_{\odot}$ (see Table 2 and Section 4.1) from Equation (7) (blue squares) and Equation (8) (red squares). The horizontal dashed line corresponds to the observed Dst_{\min} during the geomagnetic storm of 2012 March 9–11.

$-5) R_E$, the rope retreats tailward with an average velocity of $\sim 600 \text{ km s}^{-1}$. In Figures 14(c)–(f) we show the corresponding *THEMIS* B vector magnetic field data. The morphological features of the rope are as follows: first, the cross-tail B_y “core field” occurred at 11:39 UT; second, the positive-then-negative “bipolar signature” of B_z ; and third, the increased values of the simultaneous total magnetic field strength.

From 11:37 to 11:42 UT, when *THEMIS* B crosses the rope, $|B_x|$ increases from -8 to -28 nT ; that is, the satellite moves southward, from the very central plasma sheet toward the boundary region adjacent to the lobes. We know that the neutral sheet is characterized by $B_x = 0$ and the lobe domain by $B_x \simeq 30 \text{ nT}$. The polarity of the rope, given by the sign of B_y , is positive, and this is probably dictated by the southward satellite motion. The latter is in agreement with a recent suggestion by Sarafopoulos (2014), in which the present rope seems to correspond to an ion vortex, which essentially corresponds to an anticlockwise flowing current. The typical duration of the MFR structures, embedded in tailward plasma flows, is 1–2 minutes at distances 20 – $30 R_E$ (Sarafopoulos 2014). For the present, distant-tail MFR, its duration is ~ 5 minutes, from 11:37 to 11:42 UT, and its length along the tail is about $30 R_E$. We are obviously dealing with a very large entity, as also manifested by the very high level of geomagnetic activity. The core’s maximum value occurs at 11:39 UT. The observation of a magnetic flux-rope structure in the distant magnetosphere represents a clear manifestation of the change in the magnetic field topology during the substorm activity.

We now enter a more detailed discussion of the second injection event (i.e., B) of Figure 14(a). Figure 15 contains observations of *GOES*-13 energetic electrons and protons as

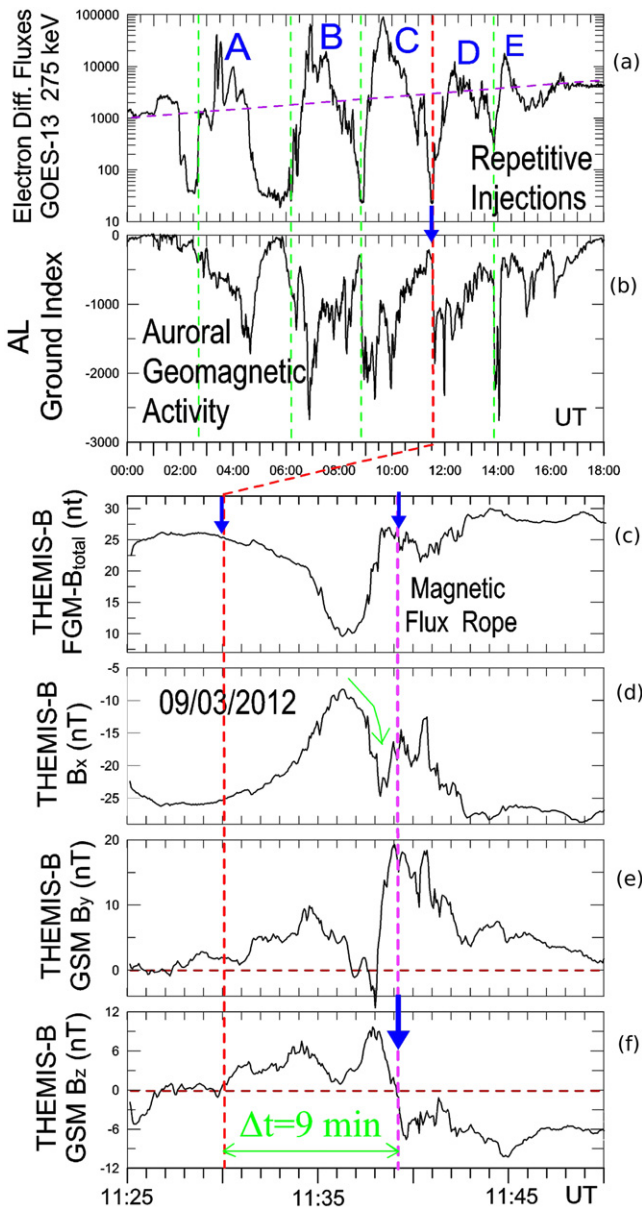


Figure 14. Panel (a) shows differential energetic-electron fluxes (275 keV) from *GOES*-13 in the geostationary orbit on 2012 March 9 (00–18 UT) and panel (b) the geomagnetic activity measured via the AL index. Five distinct injections and substorms are labeled with capital letters. The bottom four panels are vector magnetic field data measured by *THEMIS B* in the distant magnetotail; a magnetic flux-rope structure is produced and propagates tailward during the fourth substorm.

well as the magnetic field during the interval 06:00–08:00 UT on 2012 March 9. The upper panel shows *GOES*-13's flux variations of energetic protons (~ 95 to ~ 575 keV), the middle panel those of energetic electrons (~ 40 – 475 keV), and the lower panel displays *GOES*-13's magnetic field observations for the same time period. From a comparison of all the *GOES*-13 data we infer that an increase in the normal magnetic field component (B_z) from ~ 0 nT at $\sim 06:12$ UT to 100 nT at $\sim 06:54$ UT occurred along with a similar increase in the considered electron and proton energy bands that peaked at around the same time (between $\sim 06:50$ and $\sim 07:10$ UT). The onset phase of the injection event B is characterized by sudden increases in electron fluxes in different energy channels

(40–475 keV), suggesting a non-dispersive character. The observed non-dispersive onset of energetic electrons that is followed by a strongly northward turning of the geomagnetic field confirms that *GOES*-13 observed an injection event.

6.4. Radiation Belt Dynamics

The magnetospheric compression and substorm/storm dynamics caused by the shock and ICME arrival at 1 AU led to substantial changes in the strength and location of the relativistic-electron populations in the outer radiation belt. To study the relativistic-electron dynamics we calculated phase space density distributions (PSDs) using the methodology described in Chen et al. (2005) and Turner et al. (2012). The calculations were performed on phase space coordinates (PSCs) μ , K , and L^* , which are associated with the three adiabatic invariants of single-particle motions. L^* denotes the radial distance to the equatorial location where an electron crosses only in the presence of the internal dipole field. The advantage of calculating PSDs at fixed PSCs, in comparison with flux time profiles, is that it allows us to study only the effect of non-adiabatic effects on particle dynamics, i.e., to filter out adiabatic effects such as the Dst effect, which is temporal and associated with adiabatic changes due to storm-related changes in the magnetic field.

The upper panel of Figure 16 contains the electron PSD as a function of L^* for several time intervals. The calculations correspond to μ equal to 600 MeV G^{-1} and $K < 0.03 \text{ G}^{1/2} R_E$. The latter choice picks up only equatorial mirroring electrons in order to deal with the core distribution of the population. The *THEMIS D* spacecraft was inbound in the postmidnight sector ($0 < \text{MLT} < 4$, where MLT is Magnetic Local Time) during 04:00–08:00 UT (main phase of the geomagnetic storm). The energy range of the solid-state telescopes used for the PSD calculations is 350–800 keV. Lower-energy channels were ignored due to the high-level contamination by protons.

The relativistic-electron population with $\mu = 600 \text{ MeV G}^{-1}$ shows an intense dropout of PSD (orange curve) for $L^* > 4.5$ during the main phase of the storm (March 9, 04:20–06:30 UT), which is followed by enhancement of PSD. The significant compression of the magnetopause along with the extended intervals of southward B_z suggest that the main cause of the dropout is magnetopause shadowing (Kim et al. 2008; Kim & Lee 2014). On 2012 March 10 this population is enhanced above the pre-storm levels (yellow and brown curves) but the peak of the PSD distribution is now located at $6 < L^* < 6.5$ (instead of $L^* = 5.3$), indicating the existence of chorus activity which accelerates the seed population following the scenario of Horne et al. (2005).

It is well established that the power of magnetospheric ultra-low frequency (ULF) waves (roughly 1 mHz to 1 Hz, or periods 1 to 1000 s) is significantly enhanced during geomagnetic storms. At the same time, ULF pulsations play a significant role in radial-diffusion processes of energetic particles, and the power of these fluctuations has been shown to be an integral part of the radial-diffusion coefficients of energetic particles in the radiation belts (e.g., Schulz & Lanzerotti 1974; Brautigam & Albert 2000). Using simultaneous measurements from two *GOES* GEO satellites and three of the *THEMIS* spacecraft constellation during the storm of 2012 March 9–10, the power spectral density of ULF pulsations at different L -shells is calculated, as the satellites traverse different L -shells along their orbit. In the lower panels

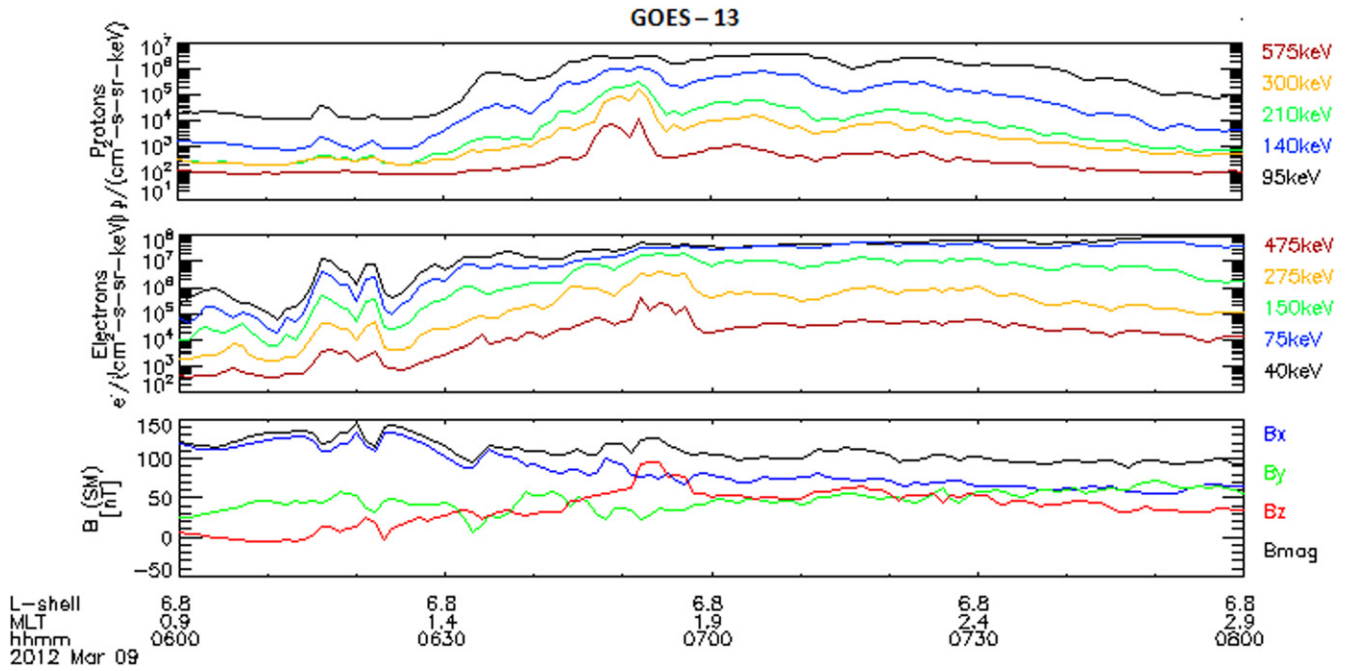


Figure 15. Anatomy of injection event B of Figure 14(a) with *GOES*-13 observations. Shown are proton (top) and electron (middle) differential fluxes in various channels, as well as the magnetic field (magnitude and components; bottom).

of Figure 16 we observe that, during storm time, ULF power in the range of Pc5 (2–7 mHz) across the magnetosphere increases by two to three orders of magnitude, leading to a corresponding enhancement of the diffusion coefficients of >300 keV electrons, and hence to enhanced outward diffusion (Mann et al. 2012; Katsavrias et al. 2015). Since ULF wave power is correlated with the solar-wind dynamic pressure (e.g., Kepko & Spence 2003; Liu et al. 2010), we can expect that the magnetospheric compression caused by the arrival of the IP shock at 1 AU (see Section 6.1) could have led to the observed enhancement of ULF waves, which in turn contributed to the observed radial losses of relativistic particles. Our results are only indicative of the change in ULF wave power during the particular event. A more detailed parametric study of wave power as a function of L and geomagnetic activity indices is currently under investigation, taking advantage of the unique configuration of the combined *THEMIS* and *Van Allen Probes* missions, in order to revisit the relationship between geomagnetic indices and radial-diffusion coefficients.

6.5. Non-extensive Dynamics of IP and Magnetospheric Plasmas

Nonlinearities in space plasma dynamics can generate intermittent turbulence with the typical characteristics of anomalous diffusion processes and strange topologies of stochastic velocity and magnetic fields caused by nonlinear MHD processes and kinetics (Zaslavsky 2002). In addition, according to Zelenyi & Milovanov (2004) the complex character of the space plasma system includes the existence of nonequilibrium (quasi)-stationary states having the topology of a percolating fractal set. The complex and non-Gaussian character of space plasmas can be explained by the non-extensive statistical thermodynamics pioneered by Tsallis, which offers a consistent and effective theoretical framework, based on a generalization of Boltzmann–Gibbs (BG) entropy, to describe nonlinear complex dynamics far from equilibrium

(Tsallis 2009). Tsallis non-extensive Statistics (TST) can be studied via the calculation of the Tsallis entropic index q , which corresponds to the maximization of Tsallis entropy S_q . This is a generalization of the standard entropy, given by

$$S_q = k \frac{1 - \sum_{i=1}^w p_i^q}{q - 1}, \quad q \in \mathbb{R}, \quad (9)$$

with k being Boltzmann’s constant and w a set of discrete p_i states. S_q measures the complexity of the system, while q measures its degree of non-extensiveness. When $q = 1$, S_q corresponds to the entropy of the usual BG statistical mechanics; $q \neq 1$ suggests deviations from the normal central-limit theorem.

To calculate q from observational time-series, the algorithm described in Karakatsanis et al. (2013) and Pavlos et al. (2014) was used. It was applied to time-series of the magnetic field magnitude recorded at various locations (see Figure 2) in both the magnetosphere (*THEMIS E* in the bow shock and *THEMIS C* in the magnetotail) and the IP medium (*Cluster* near the bow shock and *ACE* at L1). For each spacecraft, q was calculated for intervals both before (calm) and during the analyzed storm. We found that for all cases q was >1 , suggesting long-range interactions and departures from Gaussianity. In addition, and for all considered cases, q significantly increased from calm to storm times, which suggests an increase in the nonlinearity and complexity of the magnetospheric and IP medium during the storm. For example, q at L1 (*ACE*) increased from 1.37, during the calm interval from 08:54 on 2012 March 1 to 10:40 on March 4, to 1.73, during the storm interval from 10:45 on 2012 March 8 to 05:00 on March 9. This clearly encapsulates the intermittent state of the IP medium upon the arrival of the shock and ICME discussed in Section 5 and displayed in Figure 9. Based on these results, extensions of the standard MHD paradigm to include kinetic effects and incorporate the role of small-scale effects and magnetic reconnection are

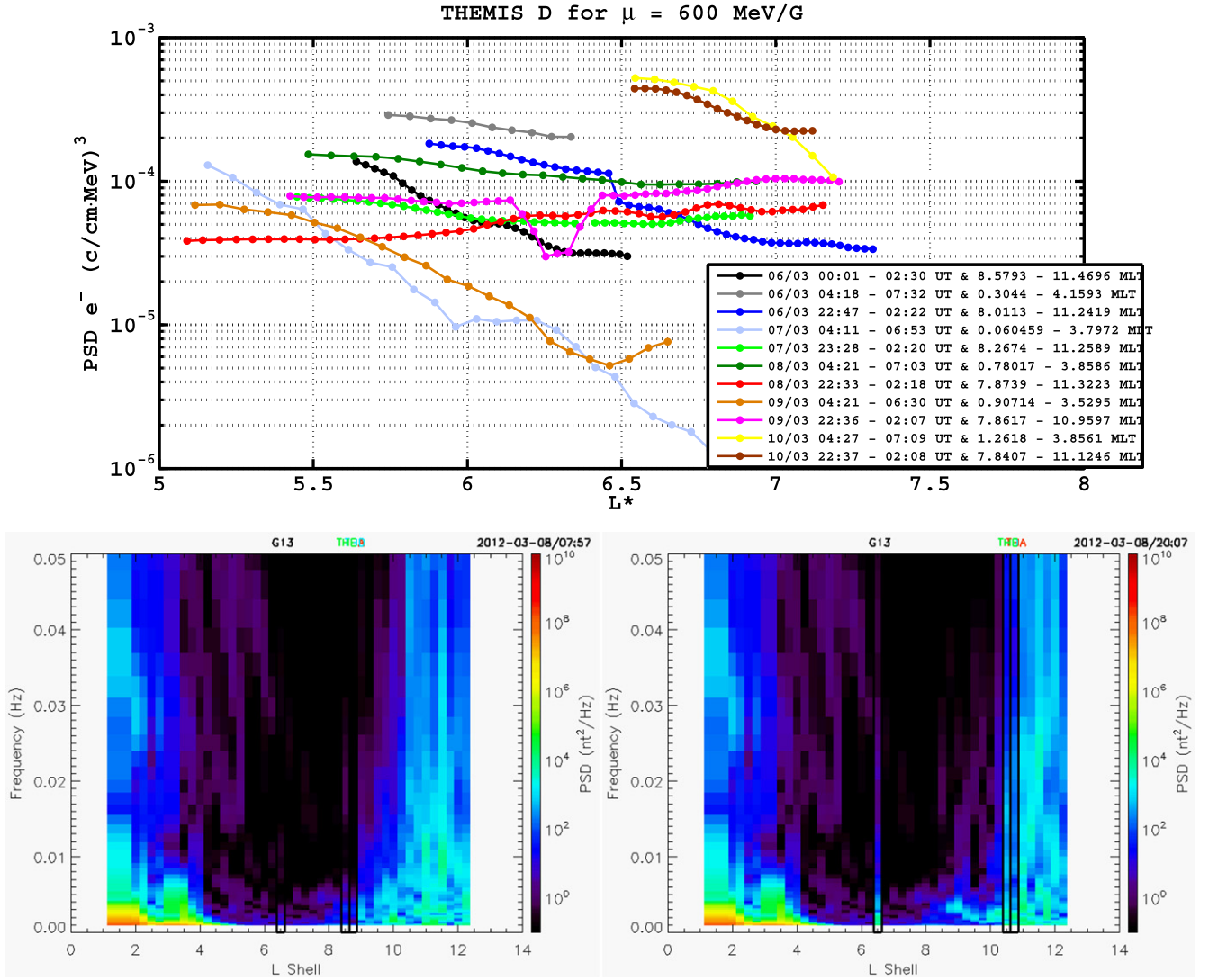


Figure 16. Upper panel: time evolution of the electron phase space density as a function of L^* for $\mu = 600 \text{ MeV G}^{-1}$ and $K < 0.03 \text{ G}^{1/2} R_E$ during the interval 2012 March 6–10, as calculated from THEMIS D data. Lower left (right) panel: ULF wave power spectral density as a function of L shell and frequency before (during) the SSC of the geomagnetic storm.

possibly warranted, in order to describe the response of the solar wind to these transient, extreme events.

7. DISCUSSION AND CONCLUSIONS

We have presented a comprehensive Sun-to-Earth study of one of the most active space weather intervals (2012 March 7–11) during cycle 24. The close temporal (~ 1 hr) and spatial (launched from the *same* AR) association of the two CMEs made the analysis particularly challenging, not only close to the Sun but also further away, when the related disturbances reached 1 AU.

Our major results can be summarized as follows.

1. Contrary to the findings of previously published works that apparently overlooked the second CME (CME2), the study of Möstl et al. (2014) and this work conclude that CME2, not CME1, was the Earth-directed event.
2. The magnetic field entrained in CME2 was estimated for the first time by means of a method combining magnetic helicity calculations in the photosphere or low corona and

geometrical modeling in the outer corona ($13 R_\odot$). The resulting magnetic field strengths of CME2 lie in the range $0.01\text{--}0.16 \text{ G}$ at $13 R_\odot$. These values are higher by a factor 8–17 than the magnetic fields of the quiescent corona.

3. Extrapolations of the inferred magnetic field of CME2 to 1 AU require steep ($\alpha_B \approx -2$) radial fall-offs to match the observed magnetic field values of the associated ICME.
4. The time of arrival and speed of CME2 at L1 are relatively well reproduced by an aerodynamic drag-force model extending from $30 R_\odot$ to 1 AU when taking into consideration the perturbed upstream conditions created by the shock associated with CME1. In this case, there was a 2 hr discrepancy between observed and modeled arrival time and a good match ($\sim 10 \text{ km s}^{-1}$) in terms of modeled and observed CME speeds.
5. The shock evolution from $30 R_\odot$ to 1 AU was modeled by a MHD simulation of a heliospheric disturbance constrained by the observations of the shock associated with CME1.

6. Using the dynamic pressure at 1 AU predicted by the observationally driven shock simulation as input to the TS05 magnetospheric model, the resulting magnetospheric compression was in qualitative agreement with observations.
7. Using the extrapolated magnetic field and speed of CME2 at 1 AU to predict Dst_{\min} , agreement was obtained with observations for a radial fall-off of B with a power-law index of ~ -2.0 .
8. The IP medium and magnetosphere exhibited a non-extensive and non-Gaussian (Tsallis q -Gaussian) character since the metastable or quasi-stationary states are described by Tsallis q -Gaussian probability distribution functions. In addition, these characteristics were enhanced during the studied storm, indicating the enhancement of the overall complexity of the system.
9. The intense relativistic-electron dropouts observed in the outer radiation belt were triggered by the strong magnetospheric compression caused by the arrival of the shock at 1 AU and the outward diffusion driven by the ULF (Pc5) wave-power enhancements.

We are encouraged by the relative success of our method of estimating the CME-entrained field and extrapolating it to 1 AU. We consider such approaches important for developing diagnostics of the near-Sun magnetic field of CMEs for assessing the geoeffectiveness of these events. Currently, very few such estimates exist (e.g., Bastian et al. 2001; Jensen & Russell 2008; Tun & Vourlidis 2013) and all of them correspond to relatively low heights ($1-7 R_{\odot}$). These estimates are based on relatively rare radio-emission configurations such as gyrosynchrotron emission from CME cores and Faraday rotation. On the other hand, our proposed methodology is based on calculations of the magnetic helicity in the lower solar atmosphere and geometrical CME modeling in the outer corona, which can both be performed on a more routine basis. Obviously, this new methodology requires further validation with a large sample of events and juxtapositions with other possible methods of inferring magnetic fields of CMEs. Two other, relatively easy-to-implement, methods aimed at inferring the CME magnetic configuration at 1 AU were recently proposed by Kunkel & Chen (2010) and Savani et al. (2015). They require flux-rope CMEs and are based on the observed kinematics, hemispheric helicity rule, and the tilt angle of the source ARs.

Some limitations exist in the MHD modeling framework used for the IP evolution of shock1 (Section 4.3): first, due to the hydrodynamic nature of the applied heliospheric disturbance, we cannot fully account for the magnetic field perturbations caused by the shock. Second, our simulation captures only part of the complexity of the IP medium during the considered interval, and therefore it is by no means a unique representation. For example, we considered only one shock, associated with CME1, but CME2 may have also driven an IP shock. In any case, our approach appears to successfully reproduce the basic, qualitative elements of the shock observations at 1 AU by using a minimal set of assumptions.

The aerodynamic prescription of CME dynamics of Section 4.3, although successful in reproducing CME arrival time and speed at 1 AU using shock-perturbed upstream solar-wind conditions, is also not unique and faces several shortcomings. For instance, one would expect that in the presence of a shock the associated turbulence may modify the

drag-force coefficient C_D from its standard aerodynamic form. In addition, the solar wind, either quiescent or perturbed, is in a turbulent state, as also demonstrated in Section 6.5, so a viscous drag may be a more appropriate description (e.g., Subramanian et al. 2012). Finally, the properties of the solar-wind turbulence could be altered in the presence of shocks (e.g., Bamert et al. 2008). In any case, it appears safe to conclude that the presence of shocks ahead of CMEs is an important contributor to their propagation (see also Corona-Romero et al. 2013). Clearly, more work is required in this important area.

We note here that the complex ICME structure at 1 AU (Section 5), together with the perturbed IP medium along its propagation path, did not allow for a more detailed empirical modeling of the Dst index (e.g., the calculation of Dst time-series). Thus we provide a calculation of a Dst proxy value only (i.e., Dst_{\min}) by making some restrictive assumptions (e.g., inclination of the CME axis). These assumptions are also incorporated in the calculations of the magnetospheric compression in Section 6.

We also stress another key outcome of this study, which is a relatively simple framework to assess the geoeffectiveness of a CME in terms of Dst index and magnetospheric compression. Our framework relies on solar/near-Sun observations and simple magnetic field and propagation models of CMEs. The complexity of the studied intervals prevented us from expanding our analysis in some areas (e.g., CME rotation from the corona to 1 AU). However, such complex intervals are also the most interesting in terms of “extreme” space weather conditions. It will be interesting to test our scheme for “simpler” events in terms of both their solar origins and their in situ geospace signatures, as this will likely place stronger constraints on all involved parameters and will, it is hoped, lead to a better reconstruction of Dst_{\min} . Finally, our framework requires further improvements in important areas such as CME propagation and evolution modeling, comparison with other available methods (e.g., those supplied by NASA’s CCMC), and obviously validation involving larger event samples.

The enhanced geoeffectiveness of events of 2012 March 7 may have been caused by the following factors.

1. *Magnetic properties of the source AR.* The photospheric magnetic field distribution of NOAA AR 11429 was unusually complex (e.g., Figure 3(b)) with uncommonly high values of various eruption-related magnetic field metrics. For example, the magnetic helicity budgets of this source region (Section 3.2; Table 2) lie at the high end of helicity distributions determined for numerous ARs (e.g., Nindos et al. 2003; Georgoulis et al. 2012; Nindos et al. 2012; Tziotziou et al. 2012).
2. *Ultra-fast CMEs close to the Sun.* CME1 and CME2 were very fast with speeds of $\sim 2000 \text{ km s}^{-1}$. Energetic-proton fluxes of gradual SEP events are correlated with the speeds of the associated CMEs, presumably due to the corresponding stronger CME-driven shocks (e.g., Kahler 2001). This may explain these extremely high proton fluxes.
3. *Non-radial propagation in the inner corona.* ICME2 would not have been Earth-directed had it erupted radially from the source region (Figure 3). Its propagation path was likely determined by the properties of the background, overlying magnetic field as well as the inferred pre-eruptive flux ropes (Chintzoglou et al. 2015).

4. *Shock preconditioning of the IP medium.* The presence of a shock ahead of CME2 had significant implications for its propagation. As shown in Section 4.3, CME2 experienced less drag compared to the case of quiescent upstream solar wind and reached 1 AU at a higher speed. The higher speed may have contributed to the enhanced Dst (see Equations (7) and (8)).
5. *Preconditioning of the magnetosphere by previous events.* Multiple ICMEs, and other related structures such as shocks and sheaths, reaching L1 with or without interaction may lead to enhanced geoeffectiveness (i.e., deeper Dst minima) of the corresponding geomagnetic storms (e.g., Burlaga et al. 1987; Daglis 1997; Farrugia et al. 2006). As discussed in Section 5 an ICME launched from 11429 on 2012 March 5 reached L1 on 2012 March 7 and gave rise to a geomagnetic storm with a minimum Dst of ≈ -90 nT (Figure 1). In addition, the B_z of the ICME in our study was first northward and then southward. This may have led to a further enhancement of the geoeffectiveness due to the accumulation of cold and dense plasma in the plasma sheet during the interval characterized by northward B_z (e.g., Lavraud et al. 2006).

Points (1), (4), and (5) above can be deduced relatively easily from pre-eruption observations. Points (2) and (3), on the other hand, require more detailed calculations involving forward modeling of the CME initiation and early propagation processes. However, to achieve meaningful space weather predictions, all factors need to be determined quantitatively; a qualitative description is not sufficient. A quantitative treatment can be achieved by either utilizing empirical relationships connecting solar, IP, and geomagnetic parameters (e.g., Kim et al. 2010; Liu et al. 2010; Park et al. 2012; Chertok et al. 2015; Papaioannou et al. 2015) or by analytical theory and modeling (e.g., Moore et al. 2007; Isavnin et al. 2013; Kay et al. 2013). Given the shortcomings of both approaches (i.e., significant scatter in empirical relationships and model limitations), *hybrid* schemes could offer a better research avenue. With the present study we propose, in a preliminary manner, such a space weather prediction scheme based on relatively easy-to-obtain photospheric and coronal observations that can be utilized by both theoretical projections and modeling. However, at this stage the entire scheme cannot be fully automated and hence it is not yet suitable for operational purposes.

We are finally looking forward to the upcoming *Solar Orbiter* (SolO) and *Solar Probe Plus* (SPP) missions and their foreseen synergies. These observations will undoubtedly supply stronger observational tests (e.g., in situ observations of CME–ICME magnetic field speed and upstream conditions both at $\sim 10 R_\odot$ by SPP and at ~ 0.3 AU by SolO when the two spacecraft are aligned) to the concepts/tools developed in this study. In addition, they will enhance our understanding of the physical processes involved in CME propagation and evolution in the IP medium.

We thank the referee for useful comments/suggestions. This research has been partly co-financed by the European Union (European Social Fund—ESF) and Greek national funds through the Operational Program “Education and Lifelong Learning” of the National Strategic Reference Framework (NSRF)—Research Funding Program: “Thales. Investing in knowledge society through the European Social Fund.” The

authors would like to thank S. K. Antiochos, V. Angelopoulos, A. Bemporad, R. Colannino, P. D  moulin, S. Dasso, P. Subramanian, B. Kliem, X. Li, and J. Zhang for useful discussions on various aspects of this work. Simulation results have been provided by the Community Coordinated Modeling Center at Goddard Space Flight Center through their public Runs on Request system (<http://ccmc.gsfc.nasa.gov>). The CCMC is a multi-agency partnership between NASA, AFMC, AFOSR, AFRL, AFWA, NOAA, NSF, and ONR. The ENLIL Model was developed by D. Odstr  il at the University of Colorado at Boulder. We also thank the CCMC/NASA personnel, in particular M. Kuhlaki and R. Evans, for their help with the ENLIL runs. We acknowledge the open data policy of the various missions and instruments used in this study. S.P. and O.P. acknowledge support from an FP7 Marie Curie Grant (FP7-PEOPLE-2010-RG/268288). M.K.G. and K.T. wish to acknowledge support from the EU’s Seventh Framework Programme under grant agreement no PIRG07-GA-2010-268245. A.V. was supported by NASA and APL funds. A.A., C.K., I.A.D., M.G., D.L.T., I.S., C.D., and G.B. acknowledge support from the European Union’s Seventh Framework Programme (FP7-SPACE-2011-1) under grant agreement no. 284520 for the MAARBLE (Monitoring, Analysing and Assessing Radiation Belt Energization and Loss) collaborative research project.

APPENDIX MAGNETIC FIELD OF CYLINDRICAL FLUX-ROPE MODELS

This Appendix describes three cylindrical flux-rope models used in the determination of the near-Sun CME magnetic fields of Section 4.1.

A.1. Axisymmetric Linear Force-free Model

We start with the well-known Lundquist flux-rope model (Lundquist 1950). This axisymmetric linear force-free solution has the following form in cylindrical coordinates (r, ϕ, z):

$$B_r = 0, B_\phi = \sigma_H B_0 J_1(\alpha r), B_z = B_0 J_0(\alpha r), \quad (10)$$

with B_0 the maximum axial field, J_0 and J_1 the Bessel functions of the zeroth and first kinds, respectively, $\sigma_H = \pm 1$ the helicity sign (i.e., handedness), and α the force-free parameter. The commonly made assumption that the first zero of J_0 is reached at the edge of the flux rope (e.g., Lepping et al. 1990) was adopted here, namely

$$\alpha R = 2.405, \quad (11)$$

with R corresponding to the flux-rope radius. This essentially leads to a purely axial (azimuthal) magnetic field at the flux-rope axis (edge).

After Equation (9) of Dasso et al. (2006) we have that the magnetic helicity H_m in a Lundquist flux rope is given by

$$H_m = \frac{4\pi B_0^2 L}{\alpha} \int_0^R J_1^2(\alpha r) dr, \quad (12)$$

with L the flux-rope length.

Solving now the above equation for the unknown axial magnetic field B_0 we get

$$B_0 = \sqrt{\frac{\alpha \Delta H_m}{4\pi L J}}, \quad (13)$$

with

$$J = \int_0^R J_1^2(\alpha R) dr. \quad (14)$$

A.2. Constant-current Non-force-free Model

The model was proposed by Hidalgo et al. (2000) and generalized by Nieves-Chinchilla et al. (2015). It is a constant-current non-force-free model with the current density components in the radial, azimuthal, and axial directions written respectively as

$$J_r = 0, J_\phi = j_\phi, J_z = j_z, \quad (15)$$

where ϕ and j_ϕ are constants. The corresponding magnetic field components are

$$B_r = 0, B_\phi = B_0 \tau_0 r, B_z = B_0(1 - r/R), \quad (16)$$

where $\tau_0 = j_z/(2j_\phi R)$ is the twist per unit length at the flux-rope axis. Finally, Equation (13) of Dasso et al. (2006) gives for B_0 that

$$B_0 = \sqrt{\frac{30H_m}{7\pi\tau_0 LR^4}}. \quad (17)$$

A.3. Linear Azimuthal Current Non-force-free Model

The model was proposed by Cid et al. (2002) and generalized by Nieves-Chinchilla et al. (2015). In this model the azimuthal current increases with distance from the flux-rope axis. The current density components are given by

$$J_r = 0, J_\phi = \alpha r, J_z = j_z, \quad (18)$$

while the magnetic field components are

$$B_r = 0, B_\phi = B_0 \tau_0 r, B_z = B_0(1 - r^2/R^2). \quad (19)$$

Finally, Equation (15) of Dasso et al. (2006) gives

$$B_0 = \sqrt{\frac{3H_m}{\pi\tau_0 LR^4}}. \quad (20)$$

REFERENCES

- Angelopoulos, V. 2008, *SSRv*, **141**, 5
- Archontis, V., Hood, A. W., & Tsinganos, K. 2013, *ApJ*, **778**, 42
- Archontis, V., Hood, A. W., & Tsinganos, K. 2014, *ApJL*, **786**, L21
- Auster, H. U., Glassmeier, K. H., Magnes, W., et al. 2008, *SSRv*, **141**, 235
- Balogh, A., Dunlop, M. W., Cowley, S. W. H., et al. 1997, *SSRv*, **79**, 65
- Bamert, K., Kallenbach, R., le Roux, J. A., et al. 2008, *ApJL*, **675**, L45
- Bastian, T. S., Pick, M., Kerdraon, A., Maia, D., & Vourlidas, A. 2001, *ApJL*, **558**, L65
- Bemporad, A., & Mancuso, S. 2010, *ApJ*, **720**, 130
- Berger, M. A. 1984, *GApFD*, **30**, 79
- Bothmer, V., & Schwenn, R. 1998, *AnGeo*, **16**, 1
- Brautigam, D. H., & Albert, J. M. 2000, *JGR*, **105**, 291
- Brueckner, G. E., Howard, R. A., Koomen, M. J., et al. 1995, *SoPh*, **162**, 357
- Burlaga, L., Sittler, E., Mariani, F., & Schwenn, R. 1981, *JGR*, **86**, 6673
- Burlaga, L. F., Behannon, K. W., & Klein, L. W. 1987, *JGR*, **92**, 5725
- Byrne, J. P., Maloney, S. A., McAteer, R. T. J., Refojo, J. M., & Gallagher, P. T. 2010, *NatCo*, **1**, 74
- Cargill, P. J. 2004, *SoPh*, **221**, 135
- Chen, Y., Friedel, R. H. W., Reeves, G. D., Onsager, T. G., & Thomsen, M. F. 2005, *JGRA*, **110**, A10210
- Chertok, I. M., Abunina, M. A., Abunin, A. A., Belov, A. V., & Grechnev, V. V. 2015, *SoPh*, **290**, 627
- Chintzoglou, G., Patsourakos, S., & Vourlidas, A. 2015, *ApJ*, **809**, 34
- Cid, C., Hidalgo, M. A., Nieves-Chinchilla, T., Sequeiros, J., & Viñas, A. F. 2002, *SoPh*, **207**, 187
- Colaninno, R. C., Vourlidas, A., & Wu, C. C. 2013, *JGRA*, **118**, 6866
- Corona-Romero, P., Gonzalez-Esparza, J. A., & Aguilar-Rodriguez, E. 2013, *SoPh*, **285**, 391
- Culhane, J. L., Harra, L. K., James, A. M., et al. 2007, *SoPh*, **243**, 19
- Daglis, I. A. 1997, *GMS*, **98**, 107
- Dasso, S., Mandrini, C. H., Démoulin, P., & Luoni, M. L. 2006, *A&A*, **455**, 349
- Davies, J. A., Perry, C. H., Trines, R. M. G. M., et al. 2013, *ApJ*, **777**, 167
- Démoulin, P., & Dasso, S. 2009, *A&A*, **498**, 551
- Escoubet, C. P., Schmidt, R., & Goldstein, M. L. 1997, *SSRv*, **79**, 11
- Farrugia, C. J., Jordanova, V. K., Thomsen, M. F., et al. 2006, *JGRA*, **111**, 11104
- Forsyth, R. J., Bothmer, V., Cid, C., et al. 2006, *SSRv*, **123**, 383
- Georgoulis, M. K., Tziotziou, K., & Raouafi, N.-E. 2012, *ApJ*, **759**, 1
- Gopalswamy, N., Akiyama, S., Yashiro, S., et al. 2015a, arXiv:1508.01603
- Gopalswamy, N., Makela, P., Yashiro, S., et al. 2015b, *JPhCS*, **642**, 012012
- Gopalswamy, N., & Yashiro, S. 2011, *ApJL*, **736**, L17
- Gosling, J. T., Eriksson, S., McComas, D. J., Phan, T. D., & Skoug, R. M. 2007, *JGRA*, **112**, 8106
- Grib, S. A., Briunelli, B. E., Dryer, M., & Shen, W.-W. 1979, *JGR*, **84**, 5907
- Grib, S. A., & Martynov, M. V. 1977, *Ge&Ae*, **17**, 252
- Gurnett, D. A., Kurth, W. S., Burlaga, L. F., & Ness, N. F. 2013, *Sci*, **341**, 1489
- Hidalgo, M. A., Cid, C., Medina, J., & Viñas, A. F. 2000, *SoPh*, **194**, 165
- Hidalgo, M. A., Cid, C., Vinas, A. F., & Sequeiros, J. 2002, *JGRA*, **107**, 10022
- Horne, R. B., Thorne, R. M., Glauert, S. A., et al. 2005, *JGRA*, **110**, A03225
- Howard, R. A., Moses, J. D., Vourlidas, A., et al. 2008, *SSRv*, **136**, 67
- Hudson, H., Fletcher, L., & McTiernan, J. 2014, *SoPh*, **289**, 1341
- Isavnin, A., Vourlidas, A., & Kilpua, E. K. J. 2013, *SoPh*, **284**, 203
- Jensen, E. A., & Russell, C. T. 2008, *GeoRL*, **35**, 2103
- Kahler, S. W. 2001, *JGR*, **106**, 20947
- Karakatsanis, L. P., Pavlos, G. P., & Xenakis, M. N. 2013, *PhyA*, **392**, 3920
- Katsavrias, C., Daglis, I. A., Li, W., et al. 2015, *AnGeo*, **33**, 1173
- Kay, C., Opher, M., & Evans, R. M. 2013, *ApJ*, **775**, 5
- Kepko, L., & Spence, H. E. 2003, *JGRA*, **108**, 1257
- Kim, K.-C., & Lee, D.-Y. 2014, *JGRA*, **119**, 5495
- Kim, K. C., Lee, D.-Y., Kim, H.-J., et al. 2008, *JGRA*, **113**, A09212
- Kim, R.-S., Cho, K.-S., moon, Y.-J., et al. 2010, *JGRA*, **115**, A12108
- Kim, R.-S., Gopalswamy, N., moon, Y.-J., Cho, K.-S., & Yashiro, S. 2012, *ApJ*, **746**, 118
- Kliem, B., Forbes, T. G., Patsourakos, S., & Vourlidas, A. 2014, *BAAS*, **224**, 21206
- Kosugi, T., Matsuzaki, K., Sakao, T., et al. 2007, *SoPh*, **243**, 3
- Kouloumvakos, A., Patsourakos, S., Nindos, A., et al. 2015, *ApJ*, submitted
- Kumar, A., & Rust, D. M. 1996, *JGR*, **101**, 15667
- Kunkel, V., & Chen, J. 2010, *ApJL*, **715**, L80
- Lario, D., Ho, G. C., Roelof, E. C., Anderson, B. J., & Korth, H. 2013, *JGRA*, **118**, 63
- Lavraud, B., Thomsen, M. F., Borovsky, J. E., Denton, M. H., & Pulkkinen, T. I. 2006, *JGRA*, **111**, 9208
- Leblanc, Y., Dulk, G. A., & Bougeret, J.-L. 1998, *SoPh*, **183**, 165
- Leitner, M., Farrugia, C. J., Möstl, C., et al. 2007, *JGRA*, **112**, A06113
- Lemen, J. R., Title, A. M., Akin, D. J., et al. 2012, *SoPh*, **275**, 17
- Lepping, R. P., Acuña, M. H., Burlaga, L. F., et al. 1995, *SSRv*, **71**, 207
- Lepping, R. P., Burlaga, L. F., & Jones, J. A. 1990, *JGR*, **95**, 11957
- Liu, W., Sarris, T. E., Li, X., et al. 2010, *JGRA*, **115**, A12201
- Liu, Y., Richardson, J. D., & Belcher, J. W. 2005, *P&SS*, **53**, 3
- Liu, Y. D., Luhmann, J. G., Lugaz, N., et al. 2013, *ApJ*, **769**, 45
- Lundquist, S. 1950, *Ark. Fys.*, **2**, 361
- Magdalenic, J., Marqué, C., Krupar, V., et al. 2014, *ApJ*, **791**, 115
- Malandraki, O. E., Lario, D., Lanzerotti, L. J., et al. 2005, *JGRA*, **110**, A09S06
- Mancuso, S., & Garzelli, M. V. 2013, *A&A*, **553**, A100
- Mann, I. R., Murphy, K. R., Ozeke, L. G., et al. 2012, *Geophysical Monograph Series 199* (Washington, DC: AGU), 69
- Mavromichalaki, H., Papaioannou, A., Gerontidou, M., et al. 2013, *JPhCS*, **409**, 012206

- McFadden, J. P., Carlson, C. W., Larson, D., et al. 2008, *SSRv*, **141**, 277
- Moore, R. L., Sterling, A. C., & Suess, S. T. 2007, *ApJ*, **668**, 1221
- Moraitis, K., Tziotziou, K., Georgoulis, M. K., & Archontis, V. 2014, *SoPh*, **289**, 4453
- Möstl, C., Amla, K., Hall, J. R., et al. 2014, *ApJ*, **787**, 119
- Nieves-Chinchilla, T., Hidalgo, M. A., Linton, M., & Vourlidas, A. 2015, *ApJ*, submitted
- Nindos, A., Patsourakos, S., & Wiegmann, T. 2012, *ApJL*, **748**, L6
- Nindos, A., Zhang, J., & Zhang, H. 2003, *ApJ*, **594**, 1033
- Odstrčil, D., & Pizzo, V. J. 1999, *JGR*, **104**, 483
- Odstrčil, D., & Pizzo, V. J. 2009, *SoPh*, **259**, 297
- Ogilvie, K. W., Chornay, D. J., Fritzenreiter, R. J., et al. 1995, *SSRv*, **71**, 55
- Ontiveros, V., & Vourlidas, A. 2009, *ApJ*, **693**, 267
- Papaioannou, A., Anastasiadis, A., Sandberg, I., et al. 2015, *JPhCS*, **632**, 012075
- Pariat, E., Nindos, A., Démoulin, P., & Berger, M. A. 2006, *A&A*, **452**, 623
- Park, S.-H., Cho, K.-S., Bong, S.-C., et al. 2012, *ApJ*, **750**, 48
- Patsourakos, S., Vourlidas, A., & Stenborg, G. 2013, *ApJ*, **764**, 125
- Patzold, M., Bird, M. K., Volland, H., et al. 1987, *SoPh*, **109**, 91
- Pavlos, G. P., Karakatsanis, L. P., Xenakis, M. N., et al. 2014, *PhyA*, **395**, 58
- Pesnell, W. D., Thompson, B. J., & Chamberlin, P. C. 2012, *SoPh*, **275**, 3
- Phan, T.-D., Paschmann, G., Baumjohann, W., Sckopke, N., & Luehr, H. 1994, *JGR*, **99**, 121
- Poomvises, W., Gopalswamy, N., Yashiro, S., Kwon, R.-Y., & Olmedo, O. 2012, *ApJ*, **758**, 118
- Richardson, I. G. 2013, *JSWSC*, **3**, A08
- Richardson, I. G., von Rosenvinge, T. T., Cane, H. V., et al. 2014, *SoPh*, **289**, 3059
- Rollett, T., Möstl, C., Temmer, M., et al. 2014, *ApJL*, **790**, L6
- Sarafopoulos, D. V. 2014, *Journal of Engineering Science and Technology Review*, **7**, 1
- Sarafopoulos, D. V., Sidiropoulos, N. F., Sarris, E. T., Lutsenko, V., & Kudela, K. 2001, *JGR*, **106**, 13053
- Savani, N. P., Owens, M. J., Rouillard, A. P., Forsyth, R. J., & Davies, J. A. 2010, *ApJL*, **714**, L128
- Savani, N. P., Vourlidas, A., Szabo, A., et al. 2015, *SpWea*, **13**, 374
- Scherrer, P. H., Schou, J., Bush, R. I., et al. 2012, *SoPh*, **275**, 207
- Schuck, P. W. 2008, *ApJ*, **683**, 1134
- Schulz, M., & Lanzerotti, L. J. 1974, *Physics and Chemistry in Space* (Berlin: Springer) 1974
- Solomon, S. C., McNutt, R. L., Gold, R. E., et al. 2001, *P&SS*, **49**, 1445
- Subramanian, P., Arunbabu, K. P., Vourlidas, A., & Mauriya, A. 2014, *ApJ*, **790**, 125
- Subramanian, P., Lara, A., & Borgazzi, A. 2012, *GeoRL*, **39**, 19107
- Syntelis, P., Gontikakis, C., Patsourakos, S., & Tsinganos, K. 2015, *A&A*, submitted
- Temerin, M., & Li, X. 2006, *JGRA*, **111**, 4221
- Thernisien, A. 2011, *ApJS*, **194**, 33
- Thernisien, A., Vourlidas, A., & Howard, R. A. 2009, *SoPh*, **256**, 111
- Tsallis, C. 2009, *Introduction to Nonextensive Statistical Mechanics: Approaching a Complex World* (New York: Springer)
- Tsironis, C., Anastasiadis, A., Katsavrias, C., & Daglis, I. A. 2015, *Ann. Geophys.*, submitted
- Tsyganenko, N. A., & Sitnov, M. I. 2005, *JGRA*, **110**, 3208
- Tun, S. D., & Vourlidas, A. 2013, *ApJ*, **766**, 130
- Turner, D. L., Angelopoulos, V., Shprits, Y., et al. 2012, *GeoRL*, **39**, L09101
- Tziotziou, K., Georgoulis, M. K., & Raouafi, N.-E. 2012, *ApJL*, **759**, L4
- Vourlidas, A., Howard, R. A., Esfandiari, E., et al. 2010, *ApJ*, **722**, 1522
- Vourlidas, A., Lynch, B. J., Howard, R. A., & Li, Y. 2013, *SoPh*, **284**, 179
- Vourlidas, A., Wu, S. T., Wang, A. H., Subramanian, P., & Howard, R. A. 2003, *ApJ*, **598**, 1392
- Vršnak, B., Magdalenic, J., & Zlobec, P. 2004, *A&A*, **413**, 753
- Vršnak, B., Žic, T., Falkenberg, T. V., et al. 2010, *A&A*, **512**, A43
- Wang, Y.-M., & Colaninno, R. 2014, *ApJL*, **784**, L27
- Wu, C.-C., & Lepping, R. P. 2005, *JASTP*, **67**, 283
- Yashiro, S., Gopalswamy, N., Michalek, G., et al. 2004, *JGRA*, **109**, 7105
- Zaslavsky, G. M. 2002, *PhR*, **371**, 461
- Zeitlin, C., Hassler, D. M., Cucinotta, F. A., et al. 2013, *Sci*, **340**, 1080
- Zelenyi, L. M., & Milovanov, A. V. 2004, *PhyU*, **47**, 1
- Zhang, J., Cheng, X., & Ding, M.-D. 2012, *NatCo*, **3**, 747
- Zhang, J., Richardson, I. G., Webb, D. F., et al. 2007, *JGRA*, **112**, 10102